Monthly Notices of the ROYAL ASTRONOMICAL SOCIETY

MNRAS **545,** 1–21 (2026) https://doi.org/10.1093/mnras/staf2242
Advance Access publication 2025 December 18

Thermal properties of interplanetary coronal mass ejections at 1 au and their connection to geoeffectiveness across solar cycles 23–25

Soumyaranjan Khuntia [1,2]★ and Wageesh Mishra [1,2]★

[1] *Indian Institute of Astrophysics, II Block, Koramangala, Bengaluru 560034, India*
[2] *Pondicherry University, R.V. Nagar, Kalapet 605014, Puducherry, India*

Accepted 2025 December 16. Received 2025 November 18; in original form 2025 August 19

ABSTRACT

Interplanetary coronal mass ejections (ICMEs) are major drivers of heliospheric variability and can produce prolonged disturbances near Earth. Understanding their thermodynamic evolution is crucial for assessing their heat budget and exploring how thermal states relate to their plasma dynamics and geoeffectiveness. We conduct a comprehensive statistical analysis of magnetic ejecta (MEs) over solar cycles 23, 24, and the ascending phase of 25. Leveraging a polytropic framework, we characterized the thermal state of ME based on the event-wise median proton polytropic index (Γ_p) from *in-situ* measurements at 1 au. We find that MEs are thermodynamically active and rarely evolve adiabatically or isothermally. Notably, a significant fraction (45 per cent) of MEs exhibit a heating state. Heating MEs dominate near solar maxima and exhibit strong solar-cycle modulation in Γ_p, proton temperature, and expansion speed, indicating active in-transit heating processes. Whereas, cooling MEs show a nearly constant $\Gamma_p \sim 2$ across cycles, suggesting enhanced cooling beyond adiabatic expectations and possible thermal energy retention from eruption to 1 au. Notably, the median Γ_p value increases from 1.49 (SC23) to 1.88 (SC24), indicating a shift to cooling-dominated states over successive cycles. High-impact ICMEs, predominantly heating MEs ($\Gamma_p = 0.59$), often manifest as magnetic clouds with enhanced magnetic fields, low plasma beta, pronounced sheath compression, elevated expansion, and post-ICME high-speed flows, making them the most geoeffective drivers of strong geomagnetic storms. These results establish Γ_p as a useful diagnostic of ICME thermal states, though meaningful assessment of geoeffectiveness requires combined consideration of thermal, plasma, and magnetic field properties.

Key words: Sun: corona – Sun: coronal mass ejections (CMEs) – Sun: heliosphere.

1 INTRODUCTION

Coronal mass ejections (CMEs) are large-scale eruptions of magnetized plasma from the Sun's corona that propagate through the heliosphere, often reaching Earth's orbit (near 1 au) and playing a crucial role in driving space weather disturbances (J. T. Gosling 1993; B. T. Tsurutani et al. 1988; D. F. Webb & T. A. Howard 2012; M. Temmer et al. 2023). CMEs are commonly observed close to the Sun using remote sensing instruments such as coronagraphs and heliospheric imagers. These instruments detect photospheric white light that is scattered by free electrons in the CME plasma via Thomson scattering. In addition to this, *in-situ* measurements from space-based probes provide valuable complementary information as CMEs propagate through the heliosphere. Once CMEs propagate through the interplanetary medium, they are traditionally referred to as interplanetary coronal mass ejections (ICMEs). A significant link between CMEs and ICMEs was established in 1982 when an ICME detected by Helios-1 was associated with a white-light CME (L. F. Burlaga et al. 1982). During their propagation, ICMEs interact with the ambient solar wind (SW) and the interplanetary magnetic field (IMF), and upon reaching Earth, they have potential of triggering major geomagnetic storms (GS). The arrival of an ICME is typically preceded by a shock and an associated sheath region (compressed SW plasma). The shock and sheath is often followed by an ICME having a prolonged period of southward-oriented magnetic field (B_z), which facilitates magnetic reconnection with Earth's northward-pointing field lines (N. Gopalswamy 2006; T. H. Zurbuchen & I. G. Richardson 2006; J. Zhang et al. 2007; E. Echer et al. 2008). This reconnection is the primary mechanism for transferring energy from ICME into the magnetosphere, ultimately driving geomagnetic disturbance (W. D. Gonzalez et al. 1994). Due to their significant impacts on satellite systems, communication networks, power infrastructure, and many other technological systems (T. Pulkkinen 2007; D. N. Baker 2009; M. Temmer 2021), the association between CMEs properties near the Sun and at 1 au have become a major focus in space weather research (Y. Liu et al. 2010; W. Mishra & N. Srivastava 2013; Y. Chi et al. 2016; C. Möstl et al. 2022). The fraction of time Earth remains within ICMEs is approximately 10 per cent during solar minimum, increasing to as much as 35 per cent during solar maximum (E. W. Cliver & A. G. Ling 2001). Gaining a comprehensive understanding of their kinematic, magnetic, and thermal properties is essential for improving space weather forecasting capabilities.

The identification of ICMEs is generally based on characteristic variations in several properties of the magnetized plasma (T. H.

★ E-mail: soumyaranjan.khuntia@iiap.res.in (SK); m.wageesh30@gmail.com (WM)

Zurbuchen & I. G. Richardson 2006; C.-C. Wu & R. P. Lepping 2011). A key component of an ICME is the magnetic ejecta (ME), characterized by a magnetic field that is stronger than the ambient SW and often exhibits smooth rotation (L. F. Burlaga et al. 1982); low plasma beta (the ratio of thermal pressure to magnetic pressure) and low proton temperatures (I. G. Richardson & H. V. Cane 1995); low electron temperatures (M. D. Montgomery et al. 1974); abnormal high charge state of ions (S. T. Lepri et al. 2001); and bidirectional streaming of electrons (J. T. Gosling et al. 1987). In addition, the presence of a declining flow speed profile, indicative of the expansion of ICMEs, can also be considered a key signature for their identification (C. T. Russell & A. A. Shinde 2003; T. H. Zurbuchen & I. G. Richardson 2006; L. Jian et al. 2006). However, it is important to note that none of these signatures alone is unique to ICMEs or sufficient for definitive identification (T. H. Zurbuchen & I. G. Richardson 2006; W. Mishra & L. Teriaca 2023). Magnetic clouds (MCs) represent a distinct subset of ME, characterized by low plasma beta and a smoothly rotating coherent magnetic field spanning a large angle, $\approx 180^{\circ}$ (L. Burlaga et al. 1981; L. F. Burlaga et al. 1982). The multispacecraft studies have demonstrated that the detection of such MC structures strongly depends on the spacecraft's trajectory through the ICME (H. V. Cane, I. G. Richardson & G. Wibberenz 1997; E. K. J. Kilpua et al. 2011). If the spacecraft passes far from the central axis or along the legs of the structure, the characteristic twisted magnetic configuration may not be detected, leading to the non-identification of a flux rope even if one is present. It is estimated that approximately 30–50 per cent of ICMEs observed at 1 au exhibit MC signatures that may have some variations over solar cycles (J. T. Gosling 1990; H. V. Cane et al. 1997; C.-C. Wu & R. P. Lepping 2007; W. Mishra, U. Doshi & N. Srivastava 2021). As ICMEs evolve through interplanetary space, they often undergo interactions with the ambient SW (S. Dasso et al. 2006; B. Vršnak et al. 2010; A. Ruffenach et al. 2012) or with other CMEs leading to change in their kinematics and structures (N. Lugaz & C. J. Farrugia 2014; W. Mishra & N. Srivastava 2014; W. Mishra et al. 2017; C. Scolini et al. 2020).

The SOlar and Heliospheric Observatory (V. Domingo, B. Fleck & A. I. Poland 1995), positioned at the first Lagrange point (L1), continuously tracks CMEs since 1995. Complementing this, the Solar TErrestrial RElations Observatory (STEREO: M. L. Kaiser 2005), with its heliocentric orbit, provides a unique 3D view of CME propagation. In addition to their remote sensing capabilities, both spacecraft are equipped with *in-situ* instruments, enabling multipoint measurements of CMEs as they travel through the heliosphere. Interplanetary probes such as the Advanced Composition Explorer (ACE: E. C. Stone et al. 1998) and Wind (R. P. Lepping et al. 1995; K. W. Ogilvie et al. 1995) have been instrumental in continuously monitoring the SW and IMF near Earth for over 25 yr. Several reliable ICME catalogues have been developed based on these *in-situ* measurements from ACE and Wind (I. G. Richardson & H. V. Cane 2010: hereafter RC catalogue), Wind alone (Y. Chi et al. 2016; T. Nieves-Chinchilla et al. 2018), and STEREO (L. K. Jian et al. 2018). These catalogues include ME boundaries for each ICME, serving as valuable references for large-sample statistical studies.

One of the major goals in the CME research field is to forecast their arrival time at Earth and assess their potential impact in driving the GS. The magnetic field, speed, and duration/radial sizes of CMEs have been investigated in earlier studies as they are known to be important parameters for driving GS (N. Srivastava & P. Venkatakrishnan 2004; L. Jian et al. 2006; J. Zhang et al. 2007; E. Echer et al. 2008). Since CMEs are composed of magnetized plasma, their global dynamics, including acceleration and expansion, are certainly influenced by their internal thermodynamic properties. The thermal state of ICMEs at 1 au may not directly influence their geoeffective potential, it could serve as indicators of other underlying properties responsible for driving strong storms. A better understanding of the additional plasma properties is therefore essential for improving both arrival-time predictions and the assessment of geo-effectiveness. It is required to understand if the thermal properties of CMEs close to the Sun or at 1 au have any dependency on the magnetic storm characteristics. However, our understanding of the evolution of a CME's internal thermodynamics remains limited, partly due to observational constraints. While spectroscopic observations can offer thermal diagnostics, they are generally confined to regions near the Sun and do not capture the CME's full evolution (E. Antonucci et al. 1997; A. Bemporad & S. Mancuso 2010). In contrast, *in-situ* observations, which can give a better measure of the thermal state of ICMEs, are only available at discrete heliocentric distances (T. H. Zurbuchen & I. G. Richardson 2006; I. G. Richardson & H. V. Cane 2010). Moreover, the sparse spatial distribution of spacecraft limits our ability to observe the same CME at multiple distances simultaneously (J. L. Phillips et al. 1995; R. M. Winslow et al. 2021).

To address these limitations, studies by Y. Wang, J. Zhang & C. Shen (2009), W. Mishra & L. Teriaca (2023), and S. Khuntia et al. (2023, 2024) have utilized CME's 3D kinematics and the flux rope internal state (FRIS) model to derive plasma properties, particularly the thermal state at heights (2–25 $R_{\odot}$) where no plasma measurements are available. These studies reveal that CMEs undergo multiple heat transfer phases, initially in a heat-releasing state near the Sun, transitioning into a near-isothermal heating phase between 3–9 $R_{\odot}$. This thermal evolution was modelled under the consideration of polytropic behaviour, where the pressure p (temperature T) and density ρ follow the relation $p \propto \rho^{\Gamma}$ ($T \propto \rho^{\Gamma-1}$), and Γ is the polytropic index. This approach provides a simplified yet insightful representation of CME's heating and cooling without involving the complexity of energy equation modelling. The choice of γ is crucial not only for characterizing CME plasma but also for understanding the broader coronal, SW dynamics and heat transport in the heliosphere (P. Riley et al. 2003; W. B. Manchester et al. 2004; R. T. Desai et al. 2020; J. Cao et al. 2013; Y. Liu et al. 2022; B. Kuźma et al. 2023; J. Cai et al. 2025). In many numerical studies, a fixed non-adiabatic value of γ is assumed, and it has been shown that variations in γ can significantly alter the simulated evolution of the SW and CMEs (W. B. Manchester et al. 2004; C. C. Wu, S. T. Wu & M. Dryer 2004; K. Liou et al. 2014; P. Mayank, B. Vaidya & D. Chakrabarty 2022; Y. Liu et al. 2022). Empirical estimates of the polytropic index within ICMEs typically range from 1.15 to 1.33 (V. A. Osherovich et al. 1993; Y. Liu, J. D. Richardson & J. W. Belcher 2005; Y. Liu et al. 2006), suggesting substantial local heating. Recently, S. Khuntia & W. Mishra (2025) report that both fast and slow ICMEs at 1 au exhibit near-isothermal expansion, sustained internal heating, and distinct turbulence properties, highlighting the role of Alfvénic fluctuations and intermittent structures in their evolution and local energy dissipation. Additional evidence for CME heating comes from both spectroscopic measurements near the Sun (B. Filippov & S. Koutchmy 2002; J.-Y. Lee et al. 2017; A. Reva et al. 2023) and the analysis of ion charge states at 1 au (C. E. Rakowski, J. M. Laming & S. T. Lepri 2007; S. T. Lepri et al. 2012). More recently, S. Khuntia, W. Mishra & A. Agarwal (2025) employed the FRIS model combined with *in-situ* data at 1 au to investigate the thermal characteristics of interacting CMEs which caused a great GS. Their results revealed enhanced electron cooling and a dominant heating trend in protons, suggesting complex thermodynamic interactions during CME–CME encounters. Although several studies have probed the polytropic behaviour of CMEs at specific distances or time intervals, a systematic

and comprehensive investigation of the thermal state of both ICMEs and the surrounding ambient SW at 1 au in connection to their geoeffective parameters is still limited. This motivates the present study, which aims to statistically characterize the thermal properties of ICMEs at 1 au using *in-situ* measurements.

Previous studies have investigated the geoeffectiveness of ICMEs and have established a dependency on key ICME properties such as B_z, electric field ($E_y = VB_z$), and SW dynamics pressure, both of which are crucial drivers of geomagnetic activity (E. Echer et al. 2008; I. G. Richardson & H. V. Cane 2011; M.-X. Zhao et al. 2021). The studies have also looked into the role of different drivers of GS in governing the rate, strength, growth, and recovery of storms (E. Echer et al. 2008; I. G. Richardson & H. V. Cane 2012; W. Mishra et al. 2024). Furthermore, ion charge states serve as valuable indicators for distinguishing between different types of SW and ICMEs, which may have varying probabilities of driving strong GS, even though these charge states are not causal parameters determining storm intensity (T. Henke et al. 1998; S. T. Lepri et al. 2001; M. J. Owens, M. Lockwood & L. A. Barnard 2018). This implies that ion charge states linked with the thermal state of SW/ICMEs close to the Sun may have an indirect relationship with their geoeffectiveness. The role of the ICME's internal thermodynamic state near the Earth in modulating GS intensity has received relatively less attention. Given that we are statistically analysing the thermal states of ICMEs, it becomes particularly relevant to examine whether CMEs associated with extreme GS exhibit distinct thermal characteristics compared to the broader ICME population. Since the thermodynamic evolution of a CME governs its expansion, density, and pressure gradients, it may also indirectly represent the CME's ability to efficiently transfer energy to Earth's magnetosphere and drive strong geomagnetic responses. Therefore, studying the thermal behaviour of both the CME and the surrounding SW at 1 au could offer additional insights, together with magnetic field, speed, and density, into the extreme space weather.

In Section 2, we describe the data set used for our comprehensive analysis. Section 3.1 details the annual occurrence of different ME categories over solar cycles 23–25. In Section 3, we focus on the estimation of the thermal state of ICMEs at 1 au and explore its temporal variation over the years and across solar cycles. Section 4 compares the plasma characteristics of heating and cooling MEs over solar cycles. Section 5 introduces the application of the superposed epoch analysis (SEA) technique to a large set of ICMEs to derive median plasma parameters, not only for the ICMEs but also for the surrounding ambient SW, to more effectively characterize ICME properties. Furthermore, we present SEA results for various subsets of ICMEs categorized based on parameters such as the presence of an MC, thermal state, and GS strength. Finally, in Section 6, we summarize the key findings of this study.

2 DATA

We used the OMNI database (J. H. King & N. E. Papitashvili 2005), available through NASA's Space Physics Data Facility at Goddard Space Flight Center (http://omniweb.gsfc.nasa.gov/). OMNI offers multiresolution plasma and magnetic field data from 1963 to the present, combining observations from multiple spacecraft and ground stations. The data set is time-shifted to 1 au, enabling consistent interplanetary analysis. Its long time span and consistency make it suitable for studying variations in SW plasma and the IMF across multiple solar cycles.

In this study, we utilized the continuously updated RC catalogue due to its extensive temporal coverage and inclusion of recent events, making it well suited for analysing ICME properties across solar cycles 23, 24, and the rising phase of cycle 25. This catalogue compiles ICMEs arriving at 1 au identified visually since 1996 and provides key timing information, including the onset of associated disturbances (typically marked by sudden storm commencements, SSCs) as well as the start and end times of ME intervals. Notably, the catalogue also categorizes the nature of each ME using a flag system: a value of '2' denotes a well-defined MC, '1' indicates partial MC-like characteristics, and '0' reflects an absence of typical MC features. For the purpose of this study, we treat events flagged as '1' or '0' as non-MC events to maintain a clear distinction between classic MCs and other ejecta structures.

It is important to acknowledge that various authors adopt different combinations of parameters to define ICME start and end times, leading to some degree of subjectivity in exact boundaries selection (see discussions in I. G. Richardson & H. V. Cane 2010). In particular, identifying the end of the ME is notably challenging as the expected return to pre-ICME conditions, marked by a gradual increase in temperature and a decrease in magnetic field strength, often occurs through a smooth and extended transition without a sharp discontinuity. This results in an hour of timing uncertainties for boundaries in the RC catalogue (I. Richardson & H. Cane 2024). Therefore, there will be some inherent uncertainty in estimating ICME parameters over their entire durations. However, our focus is not only to find the average properties of individual events but also to find the average properties over many events. It is expected that small uncertainties in defining individual ICME boundaries will average out in the statistical analysis involving multiple ICMEs.

3 THERMAL STATE OF MAGNETIC EJECTA AT 1 AU OVER SOLAR CYCLES 23–25

3.1 Annual occurrence of ICMEs and their types

A brief overview of the occurrence of ICMEs and their types provides helpful context on the distribution of events across solar cycles. Fig. 1(a) shows the annual number of ICMEs from 1996 June to 2024 December, along with the yearly mean sunspot number. A total of 604 ICMEs have been identified at Earth, as recorded in the RC catalogue. As expected, a strong positive correlation (Pearson coefficient = 0.83) is observed between ICME occurrence and solar activity. For instance, only three ICMEs were identified during the solar minimum of 1996, compared to 51 in 2000 and 48 in 2001. This upward trend is mostly consistent, except for a notable dip in 1999. The reduced ICME rate that year, also reported by H. V. Cane, I. G. Richardson & O. C. St. Cyr (2000), is attributed to an increased presence of corotating high-speed streams from low-latitude coronal holes and a restructuring of the near-ecliptic SW (J. G. Luhmann et al. 2002; I. G. Richardson, H. V. Cane & E. W. Cliver 2002). This shift in SW conditions led to a temporary decrease in CME-related activity detected near Earth (H. V. Cane & I. G. Richardson 2003). Moreover, C. C. Wu, R. P. Lepping & N. Gopalswamy (2006) reported that an unusually large heliospheric current sheet (HCS) tilt angle and high-latitude prominence eruptions in 1999 likely reduced the number of Earth-directed CMEs. Compared to solar cycle 23 (SC23), the number of ICMEs decreased in SC24. This is also shown in several earlier studies confirming the weaker SC24 than the SC23 in terms of CME occurrence rate, mass-loss rate via them, their expansion speeds, and geoeffective parameters at 1 au (N. Gopalswamy et al. 2015; W. Mishra et al. 2019, 2024; N. Gopalswamy, S. Akiyama & S. Yashiro 2020). Although the sunspot numbers in solar cycle 25 (SC25) are more comparable to SC23 and clearly higher than SC24,

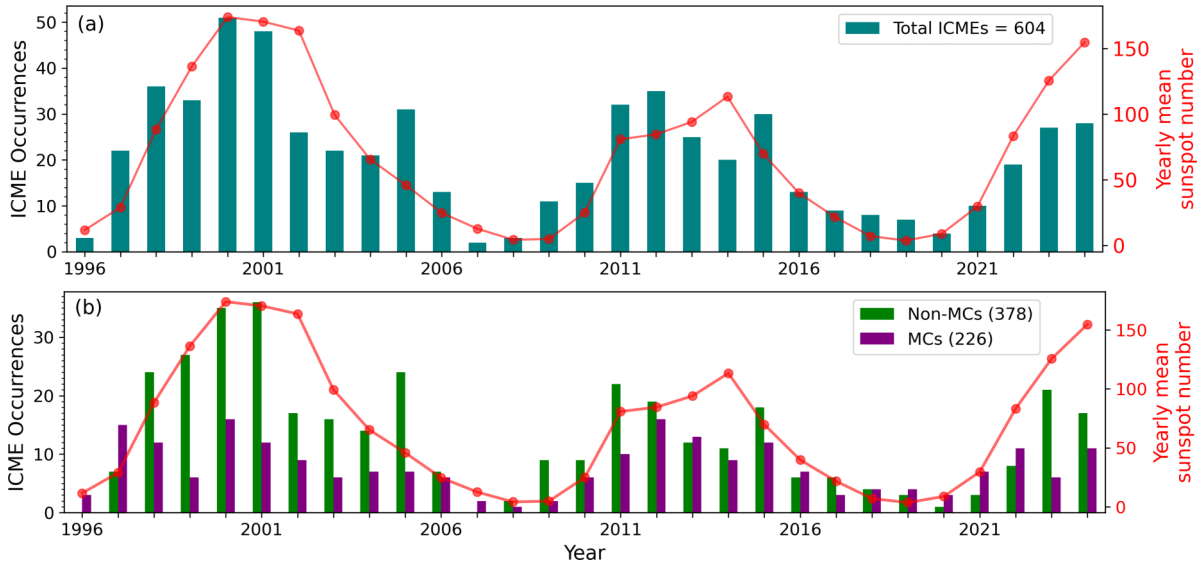

Figure 1. Annual occurrences of (a) ICMEs and (b) MC and non-MC events across solar cycles 23, 24, and the rising phase of 25. Yearly mean sunspot numbers are overplotted in both panels for comparison with solar activity levels.

the ICME count during the rising phase of SC25 appears more similar to that of SC24.

As discussed in Section 2, we classify the ICMEs into two categories: MC and non-MC. Over the study period, we identified a total of 226 MC events and 378 non-MC events. Fig. 1(b) shows their annual distribution. While SC23 had more non-MCs, SC24 showed a more balanced distribution. Interestingly, the number of MCs remained relatively constant across SC23 and SC24 and did not strongly correlate with sunspot number (Pearson coefficient = 0.62 for MCs versus 0.82 for non-MCs). This supports previous results that MCs are more common during solar minimum (H. V. Cane & I. G. Richardson 2003; L. Jian et al. 2006; I. G. Richardson & H. V. Cane 2010; W. Mishra et al. 2021), likely due to the interaction between CMEs and other structures, such as HCS, which can alter the characteristics of MCs, and is less common during solar minimum (C.-C. Wu & R. P. Lepping 2015).

3.2 Measurement of polytropic index at 1 au from *in-situ* measurements

We used 1-min resolution proton number density (N_p) and temperature (T_p) data from the OMNI database, accessed via the *Coordinated Data Analysis Web (CDAWeb): https://cdaweb.gsfc.nasa.gov/*, to estimate the proton polytropic index (Γ_p). This index was derived by performing a linear fit between log T_p and log N_p and evaluating the fit quality using the Pearson correlation coefficient (CC) and p-value (p). To enhance the reliability of Γ_p estimates, we applied this log–log fitting within moving subintervals using a 1-min step size (same as the data resolution). We tested various subinterval lengths from 3 to 10 data points and found that a 6-point window provided the highest number of statistically robust fits, defined by CC ≥ 0.8 and $p \leq 0.05$. This duration offered an optimal balance, avoiding overly short windows, which can increase statistical noise, and longer ones, which risk including multiple plasma structures, thereby weakening the correlation between T and n. This filtering approach ensures that the derived Γ_p values reflect the localized thermal state of the plasma within the ejecta and has been used in recent studies (S. Khuntia et al. 2025; S. Khuntia & W. Mishra 2025).

Fig. 2 shows the resulting Γ_p profile for an ICME, as a representative case, observed on 2010 May 28. The ME is marked by black dashed vertical lines, while the sheath region begins at the grey dashed line. For context, the plot also includes 6 h of pre- and post-ICME ambient SW. A value of $\Gamma_p = 5/3$ corresponds to adiabatic expansion with no heat exchange. $\Gamma_p > 5/3$ indicates a heat-release state, whereas $\Gamma_p < 5/3$ suggests a heating state, implying the presence of additional heating processes during plasma evolution. For this particular event, the median Γ_p value within the ME region was found to be 1.89, indicating dominant localized heat-release states. Similarly, we determined the median Γ_p value for each ME listed in the RC catalogue over the entire study period (Table A1 in Appendix A). It is important to note that in skewed distributions, the median offers a more reliable measure of central tendency than the mean, as it is less affected by extreme outlier values. Given that the Γ_p distributions in each event are generally skewed in our study, the median value more accurately captures the typical thermal behaviour of MEs.

Furthermore, since the estimation of Γ_p is based on the slope of the linear relationship between log T_p and log N_p, any measurement uncertainty in T_p or N_p propagates directly into the derived Γ_p. For 1-min OMNI Level-2 data, these fractional uncertainties vary with time and instrument calibration, typically within $\delta N_p = 2$–3 per cent and $\delta T_p = 2$–8 per cent (J. H. King & N. E. Papitashvili 2005; J. C. Kasper et al. 2006). To quantify their impact on the derived Γ_p, we performed a Monte Carlo perturbation analysis by adding Gaussian noise with $\delta N_p = 2$ per cent and $\delta T_p = 5$ per cent to the measured quantities. For each 6-point window, Γ_p was recalculated 1000 times, and the standard deviation of the resulting distribution was taken as the 1σ uncertainty for that window. The median of all window-level uncertainties within ME was adopted as the representative event-level uncertainty, reported in the seventh column of Table A1. Considering all 598 events, the overall median uncertainty in Γ_p is found to be 0.41. An example of this propagation is shown for the 2010 May 28 ICME in Fig. 2, where the window-wise uncertainties are plotted as error bars, yielding a median uncertainty of 0.45 for the event. As expected, larger measurement errors in T_p and N_p result in correspondingly higher uncertainty in Γ_p (G. Nicolaou, G. Livadiotis & R. T. Wicks 2019; G. Nicolaou et al. 2020).

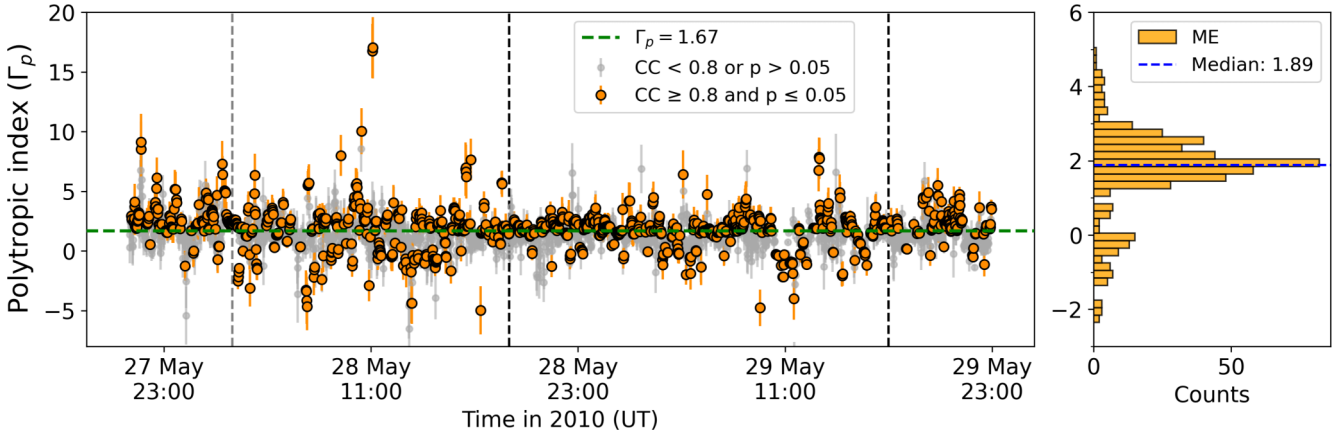

Figure 2. Derived Γ_p values across the ICME event on 2010 May 28. The grey dashed vertical line marks the start of the sheath region, while the black dashed vertical lines denote the boundaries of ME. Orange dots represent reliable Γ_p values, whereas grey dots indicate less reliable estimates. The error bars represent the uncertainty due to measurement uncertainty in N_p and T_p. The green dashed horizontal line marks the adiabatic index ($\Gamma_p = 5/3$) for reference. The right panel shows the histogram of reliable Γ_p values within ME.

Some fraction of windows exhibit negative values of Γ_p, as seen in Fig. 2. Physically, such values do not correspond to a classical thermodynamic state but rather indicate an inverse relationship between plasma pressure and density, where the pressure (or temperature) increases as the density decreases. This behaviour can arise when non-adiabatic or magnetically dominated processes govern the local plasma dynamics within an ICME. In particular, negative Γ_p values may occur in regions where magnetic tension or flux-rope expansion redistributes plasma in a way that the thermal pressure locally decreases despite compression, or where continuous energy injection (e.g. from turbulence, wave–particle interactions, or reconnection-driven heating) preferentially enhances the temperature in lower density regions. Hence, negative Γ_p values are interpreted not as physically negative thermodynamic indices but as indicators of strongly non-equilibrium, magnetically controlled, or anisotropic energy exchange within the CME-SW system. Their occurrence marks intervals where classical adiabatic or isothermal assumptions fail and where the coupling between magnetic tension, expansion, and thermal energy exchange is most dynamic.

3.3 Yearly variation of ME's thermal state at 1 au

To examine the yearly variation in the dominant thermal states of MEs across solar cycles, we classified the events into two categories: (i) heating MEs (with median $\Gamma_p \leq 1.67$) and (ii) cooling MEs (with median $\Gamma_p > 1.67$). Fig. 3(a) shows the distribution of yearly occurrences of heating and cooling MEs. In SC23, during the solar maximum and decline phase, the majority of MEs exhibited a heating state. However, during the rising phase of SC23, the thermal state shifted, with a dominance of heat-release states for MEs. A similar pattern continues into the rising phase of SC24 and SC25, where a major fraction of MEs exhibits a heat-release state. Thus, it is noticeable that during the rising phases, MEs predominantly exhibit a heat-release state, whereas during the declining phases, MEs show a more balanced state or lean towards a heating state. This thermal evolution trend aligns with previous statistical studies on ME composition on SC23, which reported that elemental charge states and relative abundances tend to increase during the rising phase and remain elevated throughout solar maxima and descending phases, compared to the lower values observed during solar minima (C. Gu, S. Yao & L. Dai 2020; H. Song et al. 2021). The ionic charge states of plasma within a CME serve as a diagnostic imprint of the electron temperature in the source region (S. T. Lepri, E. Landi & T. H. Zurbuchen 2013). Since heavy ion charge states and elemental compositions are largely preserved during CME propagation (Y.-K. Ko et al. 2010; J. R. Gruesbeck et al. 2011; S. T. Lepri et al. 2012), this similarity in the trends of composition and thermal state suggests that CMEs occurring during solar maxima and descending phases originate with inherently higher electron (and possibly proton) temperatures. As these CMEs propagate to 1 au, the elevated thermal conditions at their origin likely contribute to the observed heating states in protons, indicating a strong linkage between the CME source environment and their thermal behaviour in the interplanetary medium.

The detailed classification of MEs into distinct thermal states based on the polytropic index Γ_p, major-heating ($\Gamma_p < 0.9$), isothermal ($\Gamma_p = 1.0 \pm 0.1$), heating ($1.1 \leq \Gamma_p \leq 1.57$), adiabatic ($\Gamma_p = 1.67 \pm 0.1$), and major-cooling ($\Gamma_p > 1.77$), provides more nuanced insights into their thermodynamic evolution across solar cycles (Fig. 3b). These categories represent varying thermal behaviours: major-heating implies active heating where the temperature of the ME can increase during expansion; isothermal reflects conditions where the ME maintains an almost constant temperature; heating indicates a slower temperature decrease compared to adiabatic cooling, suggestive of less energy input compare to expansion heat loss; adiabatic represents an ideal expansion with no heat exchange, leading to a temperature decrease due to expansion-related work done; and major-cooling denotes enhanced heat-loss processes where the temperature drops more rapidly than adiabatically.

In SC23, major-heating events show a clear rise during the ascending phase, from 1 in 1997 to 5 in 1998 and 11 in 1999 (Table B1). Yet, this phase is dominated by major-cooling events, particularly in 1997–1998, comprising 86 per cent and 64 per cent of total events, respectively. A shift occurs during 2000–2001, when major-heating events account for 48–60 per cent of all cases (Fig. 3b), reflecting strong CME-associated heating during peak activity. Post-maximum, counts decline sharply (12 in 2002, and 9 in 2003), but 2005 shows a resurgence to 20 events (65 per cent), indicating prolonged heating activity in the descending phase. Overall, this pattern suggests enhanced energy input into MEs during SC23, likely linked to elevated source-region plasma temperatures near solar maximum and descending phase.

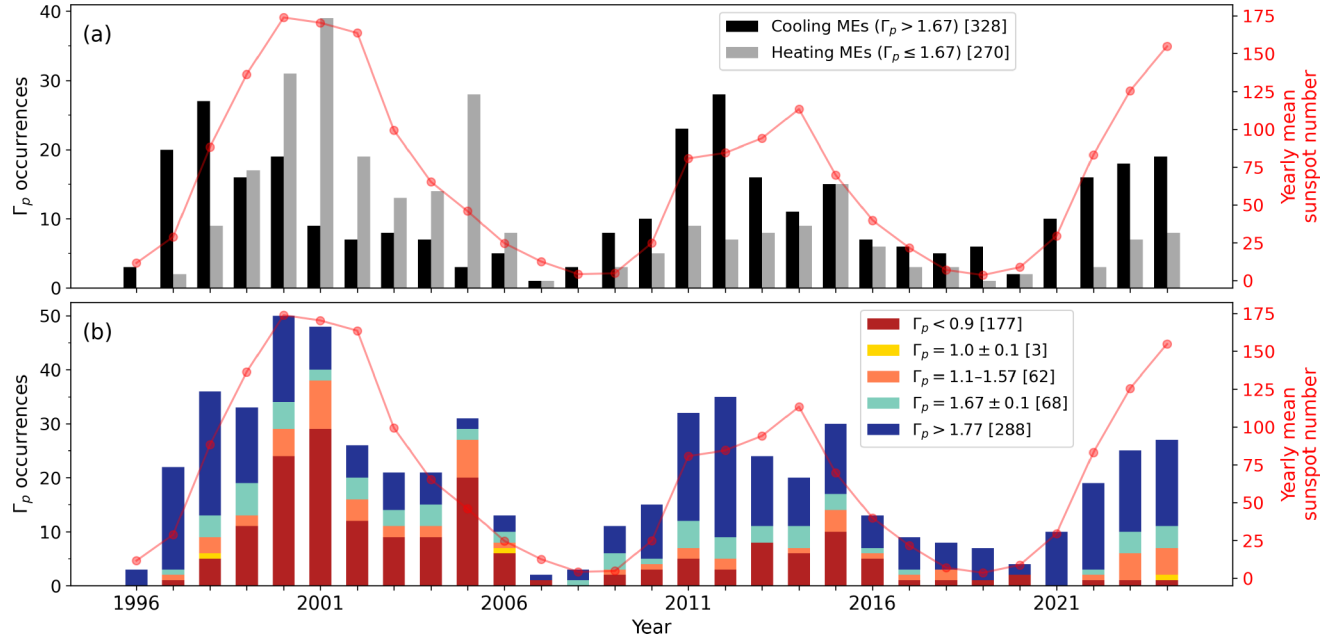

Figure 3. (a) Annual occurrence of heating and cooling ME across SC23, 24, and rising phase of SC25. (b) Annual distribution of ME with various categories depending on Γ_p values.

In contrast, SC24's ascending phase (2008–2012) is dominated by major-cooling events, peaking at 74 per cent in 2012, implying stronger heat loss or reduced heating efficiency. The 2013–2014 maximum exhibits a balanced mix of heating and cooling, unlike SC23's heating-dominated peak, which highlights the distinct thermal behaviour during the solar maxima of SC23 and SC24. This distinction could stem from the inherent properties of CMEs during their eruption or from variations in the interplanetary medium through which the CMEs propagate, which may influence their evolution and affect their thermal state at 1 au. The CMEs' expansion speeds at 1 au and the properties of the interplanetary medium during the maximum of SC23 and SC24 are found to be different in earlier studies (N. Gopalswamy et al. 2015, 2020; P. L. Lamy et al. 2019; W. Mishra et al. 2021). In the early rising phase of SC25 (2020–2024), major-cooling events remain prevalent (86 per cent in 2019, and 84 per cent in 2022), though 2023–2024 show a modest rise (24–27 per cent) in heating-related states, hinting at renewed thermal activity as the cycle strengthens. Notably, isothermal MEs are rare across all years, appearing sporadically and constituting a negligible fraction of the total, reinforcing that MEs at 1 au are typically thermodynamically active and deviate significantly from equilibrium expansion.

These results emphasize that the thermal states of MEs are not uniformly distributed across the solar cycle but are closely modulated by the phase of solar activity. The dominance of major-heating states during solar maxima and descending phases suggests stronger heating at the CME source regions, likely from flare-associated energy release or shock-driven compression, which is partly retained during heliospheric propagation. Conversely, the prevalence of major-cooling states during rising phases may reflect the emergence of CMEs with cooler coronal origins or insufficient internal energy to offset adiabatic expansion and radiative losses. Thus, this classification not only captures the thermal behaviour of MEs but also serves as a diagnostic of the large-scale thermodynamic evolution of the SW-CME system over solar cycles.

Overall, our findings suggest the coexistence of heating and cooling MEs reflects the complex thermodynamic interaction between an expanding flux rope and the surrounding SW. Heat exchange in the ME-SW system can primarily occur through a combination of adiabatic expansion, thermal conduction along magnetic field lines, and turbulent or compressive energy dissipation. During propagation, a freely expanding ME tends to cool adiabatically as its internal pressure and density decrease, corresponding to Γ_p values approaching the adiabatic limit ($\sim$5/3). However, in many cases, the derived Γ_p is significantly lower, implying net heat input into the ME plasma. The physical mechanisms responsible for such heating are not yet fully understood, but several plausible processes have been proposed. One possibility is the transfer of heat from the lower corona to the CME flux rope through its magnetic footpoints that remain connected to the Sun (D. E. Larson et al. 1997). Continuous energy injection from the ambient SW into the CME in the outer corona may also contribute, although cross-field diffusion of charged particles is expected to be strongly inhibited by the magnetic field geometry (M. Zhang, J. R. Jokipii & R. B. McKibben 2003). Magnetic energy dissipation at different heights within the CME can also contribute to heating, potentially influencing its global kinematics and expansion rate. The untwisting of the flux rope may release magnetic energy that sustains CME expansion (A. Vourlidas et al. 2000), while a portion of the internal magnetic energy could be converted into heat via Joule dissipation (j^2/σ), where j is the current density and σ is the electrical conductivity (A. Kumar & D. M. Rust 1996). Although the high conductivity of the interplanetary medium limits the efficiency of Joule heating, internal magnetic reconnection within the CME (C. J. Farrugia et al. 1993) or between the CME and the IMF (N. Lugaz et al. 2013) may still play a significant role in converting magnetic energy into thermal energy. These processes, together with conductive and turbulent energy transfer from the surrounding SW (A. Akmal et al. 2001; A. Ciaravella et al. 2001; A. Bemporad et al. 2007; J. Y. Lee et al. 2009; E. Landi et al. 2010; W. Manchester et al. 2017; M. Temmer 2021), collectively can determine whether an ME

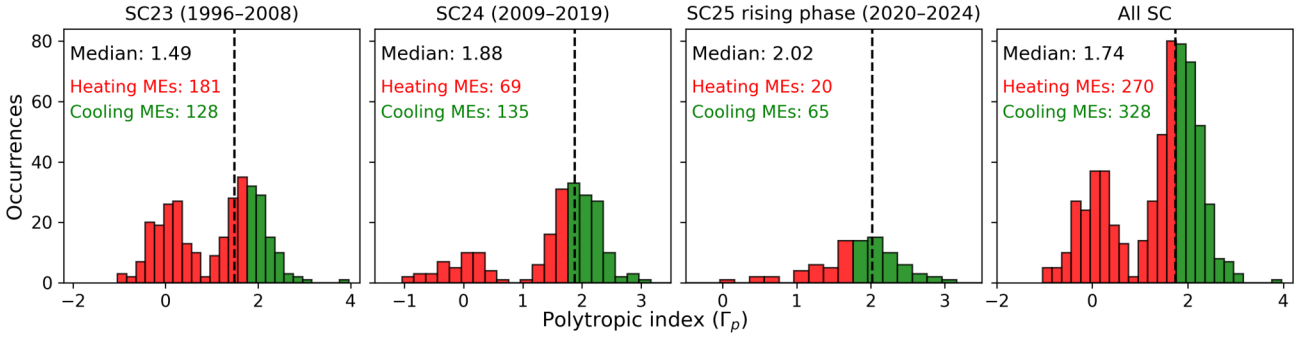

Figure 4. Distribution of Γ_p over in SC23, 24, and ascending phase of SC25.

undergoes net heating or cooling during its interplanetary evolution. This thermodynamic diversity underscores the importance of ME–SW coupling in shaping CME propagation. Therefore, future studies should focus on quantifying the heat-generation efficiency of these different mechanisms and assessing their relative contributions to the thermal evolution of CMEs throughout the heliosphere.

3.4 Solar cycle variation of ME's thermal state at 1 au

Fig. 4 presents SC variation in the distribution of median Γ_p values for each ME. In SC23, the median Γ_p value is found to be 1.49, indicating a predominance of heating MEs. Specifically, 181 out of 309 MEs (approximately 59 per cent) exhibited a heating state at 1 au. In contrast, SC24 shows a median Γ_p of 1.88, suggesting a shift toward MEs with a heat-release (cooling-dominated) state. Only 69 out of 204 MEs (about 34 per cent) showed heating characteristics during this cycle. In the rising phase of SC25, the median Γ_p further increases to 2.02, indicating an even stronger prevalence of heat-release states. Here, only 20 out of 85 MEs (around 23 per cent) exhibited heating signatures.

These results suggest a significant solar cycle dependence in the thermal state of ICMEs, with heating being more dominant during SC23 and gradually declining in SC24. The overall median Γ_p across all three solar cycle phases is 1.74, which is slightly above the adiabatic index of 5/3 (1.67). This proximity to the adiabatic limit indicates that, on average, the plasma within MEs at 1 au is neither strongly heated nor strongly cooled, although notable variations exist. Notably, 270 out of 598 MEs (approximately 45 per cent) still exhibit heating behaviour, underscoring the complexity and variability of CME thermodynamics across different heliospheric conditions. Interestingly, a recent statistical study by C. Katsavrias et al. (2025) reports a similar average polytropic index of $\Gamma = 1.63$ for MEs. Their analysis uses a different CME catalogue (T. Nieves-Chinchilla et al. 2019), spanning 1995 to 2001, along with *Wind* spacecraft data, and applies a slightly different set of filters to estimate Γ. It is worth noting that their value represents an average, whereas our study focuses on the median of the Γ distribution. In our study, we notice a clear bimodal distribution in Γ_p, with a noticeable dip around $\Gamma_p = 1$ (Fig. 4), consistent with the findings of C. Katsavrias et al. (2025). However, isolating the true isothermal state is challenging due to filtering effects that can distort the underlying distribution. Such filtering can artificially suppress tails or create enhanced dips near $\Gamma_p = 1$, which may be further exaggerated by parametric fitting approaches (e.g. Gaussian or κ-Gaussian), as these impose rigid functional forms that may not reflect the true complexity of the ICME data. To mitigate these issues, we adopt a non-parametric, assumption-free approach by using the median and its bootstrap-derived uncertainty to characterize the central tendency of Γ_p. Unlike parametric fitted estimates, the median is robust to skewness and local depletions, as it relies only on rank ordering rather than density within narrow intervals. This ensures that, unless filtering drastically affects values near the central rank (which is not the case in our data), the median remains a stable and unbiased measure. Overall, this methodology allows for a more reliable interpretation of thermodynamic variability across ICMEs, particularly in the presence of filtering artefacts and deviations from unimodality.

We find that CME thermodynamics are modulated by solar cycle activity, with variations likely arising from differences in CME initiation mechanisms, coronal background conditions, and CME–SW interactions. However, it remains challenging to determine which of these factors primarily governs the thermal state of MEs observed at 1 au. Previous studies have shown that a higher fraction of CMEs in SC24 originated from non-active region (non-AR) sources, such as filament eruptions from quiet Sun regions and higher latitudes, compared to SC23 (N. Gopalswamy, S. Yashiro & S. Akiyama 2016; P. L. Lamy et al. 2019; W. Mishra et al. 2019). Additionally, the expansion behaviour of ICMEs differed significantly between the two cycles due to a reduced heliospheric background pressure in SC24 (N. Gopalswamy et al. 2020; W. Mishra et al. 2021). This enhanced expansion likely contributed to the observed cooling-dominated thermal state during SC24. There is also a possibility that the MEs were inherently different at the time of the eruption, depending on their source regions or associated flare characteristics (J. Oloketuyi, Y. Liu & M. Zhao 2019; J. Lin et al. 2023; K. Pandey et al. 2023). Furthermore, the frequency and intensity of GS were markedly lower in SC24 compared to SC23, which may be a reflection of less energetic CME events during that cycle (W. Mishra et al. 2024). These factors together offer a plausible explanation for the transition from heating- to cooling-dominated MEs from SC23 to SC24.

4 VARIATIONS IN PLASMA PROPERTIES OF HEATING AND COOLING MAGNETIC EJECTA

We classified MEs into two categories based on their Γ_p values: heating MEs ($\Gamma_p < 1.67$) and cooling MEs ($\Gamma_p > 1.67$). For each category, the yearly median Γ_p was computed (Fig. 5a). We found that cooling MEs consistently exhibit a median $\Gamma_p \approx 2$ with minimal year-to-year variation, whereas heating MEs show substantial variability but no clear correlation with solar activity (represented by annual sunspot numbers). During SC23, Γ_p for heating MEs decreases from the ascending phase to solar maximum and remains nearly constant during the descending phase, consistent with the enhanced occurrence of heating MEs in those periods (Fig. 3). In SC24, Γ_p for heating MEs initially rises in the ascending

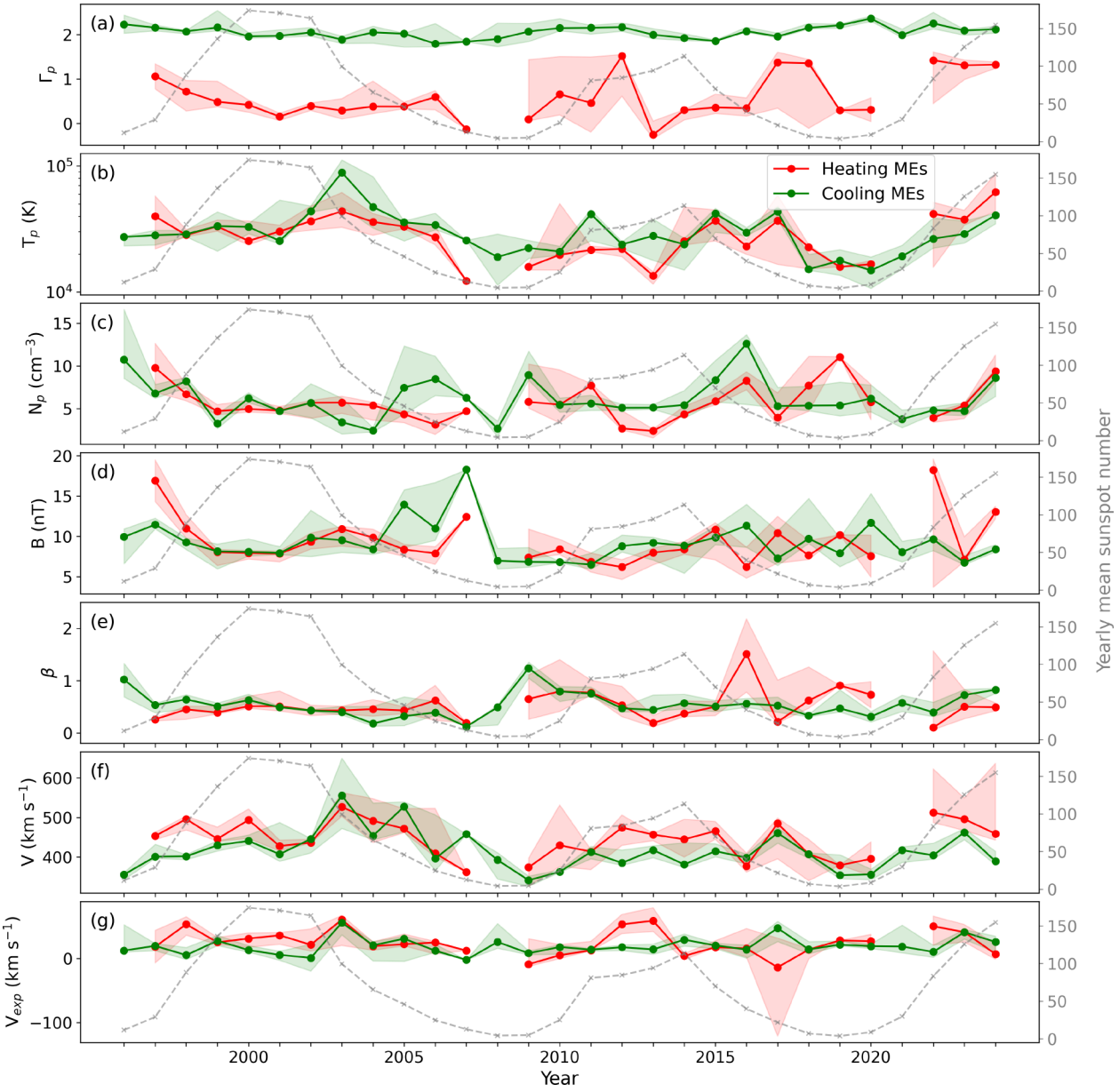

Figure 5. Yearly median values of (a) polytropic index (Γ_p), (b) proton temperature (T_p), (c) proton number density (N_p), (d) magnetic field strength (B), (e) plasma beta (β), (f) bulk speed (V), and (g) expansion speed ($V_{\rm exp}$) for heating and cooling MEs across solar cycles 23, 24, and the ascending phase of cycle 25. The background colour-shaded regions represent the 68 per cent (1σ) confidence intervals obtained via bootstrap resampling. Each panel is overplotted with the yearly mean sunspot numbers to investigate the correlation between solar activity and the thermal, plasma, and magnetic properties of MEs.

phase, drops sharply around the 2013 maximum, and then gradually increases toward the 2018 minimum. In the rising phase of SC25, Γ_p remains nearly constant, close to an isothermal state. Overall, heating MEs exhibit stronger heating (lower Γ_p) during solar maxima and descending phases, while during solar minima (e.g. 2008 and 2021), only Cooling MEs are observed with $\Gamma_p \approx 2$, indicating dominant heat loss.

Fig. 5(b) shows the yearly median T_p values for both ME categories. For cooling MEs, T_p remains nearly constant through the ascending and maximum phases of SC23, rises slightly during the early descending phase, and then declines toward the 2008 minimum. A similar but more irregular trend appears in SC24, with T_p increasing through the ascending and maximum phases and decreasing thereafter. Starting from the deep minimum in 2008, T_p rises gradually until 2017, falls in 2018, and then increases again through the rising phase of SC25. This long-term variation reflects solar cycle modulation, higher temperatures during active phases, and lower values during minima, consistent with earlier findings (Y. Chi et al. 2016; L. K. Jian et al. 2018), which reported higher SW temperatures during active phases and lower values during minima.

Heating MEs display a broadly similar trend in T_p as cooling MEs, with a rising pattern during the ascending, maximum, and early descending phases, followed by a declining phase. However, certain interesting differences are evident. Notably, in 2013, Fig. 5(a) shows a significantly lower Γ_p value for heating MEs, indicating stronger thermal heating during propagation. Yet, the *in-situ* measured T_p for the same year is lower compared to neighbouring years. This observation highlights an important physical insight: the *in-situ*

measured T_p is a combined result of the initial eruption temperature of the ME and the subsequent heating it experiences during its interplanetary journey. Thus, despite stronger in-transit or ongoing heating (as suggested by the low Γ_p), the lower T_p implies that the MEs erupted with a relatively cooler initial temperature in 2013. A similar behaviour is noticed during solar minima years like 2007–2009 and 2019–2020, where Γ_p values are lower (indicating more heating), but T_p is also relatively low. This suggests that during solar minima, MEs generally erupt with lower inherent temperatures, likely due to weaker solar activity with lower CME energetics (A. Vourlidas et al. 2011; N. Gopalswamy et al. 2014; P. L. Lamy et al. 2019; V. Pant et al. 2021). Thus, while heating processes during propagation contribute significantly to the thermal state of MEs, the initial temperature at eruption, strongly modulated by solar activity levels, plays a crucial role in determining the final *in-situ* observed T_p. Furthermore, when we compared the annual median T_p between heating and cooling MEs during SC23 and SC24, we found that the cooling MEs generally exhibit higher T_p values than the heating MEs. In contrast, during the ascending phase of SC25, the heating MEs show higher T_p compared to the cooling MEs. This change may reflect a shift in the source region properties or heliospheric conditions between SCs.

Fig. 5(c) presents the yearly median values of N_p for heating MEs and cooling MEs. During SC23, cooling MEs exhibit a generally declining and somewhat irregular trend in N_p throughout the ascending, maximum, and early descending phases, continuing until 2004. From 2005 to 2007, N_p displays an enhanced level, followed by a notable decrease during the deep solar minimum in 2008. In SC24, N_p for cooling MEs shows a clear rising trend from 2008 to 2016, reaching a peak around 14 cm^{-3}. After this peak, N_p maintains a relatively stable level until 2020. A slight decrease is observed afterward, followed by a renewed increase during the ascending phase of SC25. In contrast, heating MEs exhibit a comparatively smoother evolution in N_p during SC23, with a gradual decline observed up to 2006. Entering SC24, N_p values appear elevated compared to SC23 during the ascending phase but reach a minimum around the solar maximum in 2014. Following this dip, N_p steadily increases up to 2019, with a minor drop occurring in 2017. After 2019, N_p values again decreased slightly, but from 2022 onward, a renewed increasing trend is evident during the rising phase of SC25. Overall, heating MEs have consistently lower values of N_p compared to cooling MEs.

Fig. 5(d) shows the yearly median values of B for heating and cooling MEs. For cooling MEs, B declines during SC23's ascending and maximum phases, then rises irregularly through the descending phase, peaking near ∼18 nT around the 2007 minimum. In SC24, for cooling MEs, B increases smoothly from 2008 to a peak of ∼11 nT in 2016, then decreases toward SC25. Heating MEs exhibit more distinct cycle-dependent variations: B falls sharply during SC23's early ascent, stabilizes near the maximum, increases slightly during 2001–2003, and rises sharply again near the 2007 minimum. In SC24, B increases from ascent to early descent (peaking around 2015) and remains elevated compared to earlier cycles. In SC25, heating MEs exhibit elevated and fluctuating B values that are generally higher than those seen in SC24. Overall, the long-term variation of B does not exhibit a clear and systematic solar cycle dependence for either category. However, it is noteworthy that both categories tend to exhibit their maximum B values during the descending phases of the solar cycles. Furthermore, the B profiles of heating and cooling MEs are broadly similar in magnitude and variability across the solar cycles, suggesting common underlying physical drivers modulating the magnetic field strength of MEs over time.

We observe a reversal trend in β for heating and cooling MEs during SC23 (Fig. 5e). Specifically, β decreases gradually for cooling MEs, while it increases steadily for heating MEs from the ascending to the descending phase of SC23. During the solar minimum around 2007–2009, β for cooling MEs shows an increasing trend. However, during SC24, β again decreases from the ascending to the descending phase for cooling MEs. Unlike the behaviour before SC24, we do not observe a significant rise in β during the solar minimum between SC24 and SC25. In SC24, during the solar maximum, cooling MEs exhibit a higher β compared to heating MEs. However, during the descending phase of SC24, the heating MEs show a higher β than the cooling MEs.

Across all SCs, we found that V increases gradually during the ascending phase and solar maximum, peaking around the early descending phase before decreasing towards the solar minimum for both heating and cooling MEs (Fig. 5f). Notably, during the ascending and maximum phases, heating MEs generally exhibit higher flow speeds compared to cooling MEs. This suggests that heating MEs during these phases are associated with more energetic eruptions. Moreover, $V_{\rm exp}$ of MEs also shows interesting behaviour across SCs (Fig. 5g). During solar maxima, heating MEs tend to have higher expansion speeds compared to cooling MEs. In particular, for the year 2013, we observe a notable case: despite a lower T_p and lower Γ_p (indicating enhanced heating), $V_{\rm exp}$ is higher. This suggests that even though the internal thermal energy of the ME was relatively low (low T_p), the outward expansion was significant, likely supported by a strong internal magnetic pressure or a higher eruption energy at the source region.

5 SUPERPOSED EPOCH ANALYSIS APPLIED TO ICME

We employed the SEA technique to statistically determine the average temporal evolution of plasma parameters and geomagnetic indices associated with different categories of ME events. SEA aligns multiple events to a common reference time, typically the event start time, and normalizes their durations, allowing characteristic features to emerge by averaging (or taking the median) across events. This approach highlights common trends but may mask individual variations. We use the SEA as a statistical method to determine averaged profiles of physical parameters for the normalized duration of the events. SEA is a widely used technique in space physics and has been applied to study the SW and ICME (G. Zhang & L. F. Burlaga 1988; R. M. Winslow et al. 2015; J. J. Masías-Meza et al. 2016; M. Janvier et al. 2019; F. Regnault et al. 2020; X. Guo et al. 2021).

To perform SEA, we first normalized the time-series of each event (i.e. ME) so that the sheath start time (or the disturbance time as in the RC catalogue) and the start and end times of ME are mapped onto a common, standardized time-scale. This normalization ensures that different events, which may naturally have different durations, can be meaningfully compared on the same timeline. Since MEs size is found to be about three times that of the sheath at 1 au (J. Zhang, W. Poomvises & I. G. Richardson 2008; J. J. Masías-Meza et al. 2016; W. Mishra et al. 2021), we assigned different normalized time ranges: we divided the sheath interval into 25-time bins and the ME interval into 75-time bins. This choice preserves the typical size ratio between the sheath and ME regions. In addition to the sheath and ME regions, we also included two more intervals: a pre-ICME SW region (before the sheath) and a post-ICME wake region (after the ME). The durations of these intervals were made equal to the sheath and ME durations, respectively. After the normalization, we divided the time-series of

each ME into an equal number of bins. This is important because each ME event has a different duration and a different number of recorded data points. By binning the data, we ensure that each ME contributes equally to the final profiles. Finally, for each individual time bin across all MEs events, we calculated the median values of the studied parameters, such as magnetic field strength, plasma properties, and dynamic pressure. This method allows us to extract the average behaviour of ME structures and their surrounding regions by emphasizing common patterns while minimizing the effect of event-to-event variability.

To thoroughly evaluate differences in the thermodynamic behaviour, specifically in the distributions of Γ_p, across different classes of ICMEs, we also employed a comprehensive set of statistical methods. The *Kolmogorov–Smirnov (KS) test* was used to detect differences in the overall shape and cumulative distribution of Γ_p; a test statistic $D > 0.1$ combined with a p-value less than 0.05 is generally taken as strong evidence that the distributions differ significantly in form. The *Mann–Whitney U test*, a non-parametric test, evaluates whether one distribution tends to produce higher or lower values than another without assuming Gaussian behaviour; a p-value less than 0.05 similarly indicates a statistically significant difference in central tendency (e.g. medians). To quantify the magnitude and direction of this difference, we used *Cliff's delta*, which quantifies the effect size by measuring the probability that a randomly selected Γ_p value from one group will exceed that from another; values near zero indicate substantial overlap between the two distributions, while values approaching ± 1 suggest nearly complete separation, with one group consistently exhibiting higher or lower values than the other. In addition, we examined the *percentage of time bins* in the SEA where the median Γ_p fell below a critical threshold ($\Gamma_p < 1.67$), providing insight into the temporal extent and frequency of enhanced heating. Finally, we applied a *permutation test* on the median Γ_p values, which involves randomly reassigning group labels to build a null distribution; if the observed difference lies in the extreme tail (e.g. $p < 0.01$), it strongly suggests the difference is not due to random variation. Together, these complementary tests allow us to assess not only whether two populations differ, but also how strong, localized, and statistically robust those differences are.

5.1 Evolution in plasma properties across MEs (MCs and non-MCs)

To investigate the typical behaviour of plasma and magnetic field parameters during ICMEs, we performed the SEA using 604 ICMEs from the RC catalogur. As discussed before, these events were categorized into MCs (flag 2) and non-MCs (flags 0 and 1), with 226 MCs and 378 non-MCs. Fig. 6 presents the median profile of parameters such as Γ_p, T_p, N_p, β, B, V, $P_{\rm dyn}$, and Sym-H in each time bin. The shaded regions in the figure indicate the 68 per cent (1σ) confidence intervals for the median values, which were estimated using a non-parametric bootstrap resampling technique (with 1000 iterations). These confidence bands provide a robust, data-driven measure of the statistical variability of the median profiles, accounting for sample dispersion within each time bin. Table 1 provides the median values of these parameters for each region, pre-ICME, sheath, ME, and post-ICME, across different event categories.

We found that Γ_p exhibits a distinct four-phase pattern. For all ICMEs, the median Γ_p is highest in the pre-ICME region (2.02), dips to 1.83 in the sheath, reaches its lowest in the ME (1.73), and then recovers to 1.91 in the post-ICME region (Table 1). This behaviour indicates a transition from an enhanced cooling state to near-adiabatic expansion in the ME, followed by an enhanced cooling state again. The same trend holds for MCs and non-MCs individually, with MCs having slightly higher Γ_p in pre (2.09) and slightly lower in post (1.88) regions compared to non-MCs (1.95 and 1.93, respectively). The comparison between MCs and non-MCs reveals a statistically significant, but very subtle, difference in their Γ_p distributions. The KS test yields $D = 0.030$ with a highly significant p-value ($p \approx 1.38 \times 10^{-47}$), indicating a detectable difference in distribution shapes. However, the effect size is small, as supported by Cliff's Delta of -0.009, which implies that a randomly selected non-MC event has a slightly higher Γ_p than an MC in only 50.4 per cent of cases. The Mann–Whitney U test similarly returns a small p-value ($p \approx 2.26 \times 10^{-4}$), reinforcing the statistical significance but not the practical significance. A permutation test on the median Γ_p values further confirms this pattern: the observed median difference between MCs and non-MCs is small ($\Delta\Gamma_p = -0.0519$), yet highly significant ($p < 10^{-5}$). The KDE (kernel density estimates) plot (Fig. C1a) confirms this: both distributions show nearly identical bimodal structures across the full range of Γ_p. The MCs and non-MCs peak similarly around $\Gamma_p \approx 2$, and their overall shapes and tails are closely aligned. These results suggest that although the large sample size detects a statistical difference, the thermodynamic properties inferred from Γ_p are largely comparable between MCs and non-MCs. This implies that factors other than MC topology may play a more dominant role in shaping the compressive or heating characteristics of ICMEs.

Furthermore, T_p reveals the highest value in the sheath and the lowest values inside the ME (Fig. 6b). For all ICMEs, the sheath has the highest median T_p of 11.5×10^4 K, while the ME has the lowest at 3.0×10^4 K. This indicates that the compression and turbulence in the sheath significantly increase the plasma temperature, while the ME undergoes substantial cooling due to expansion. When comparing MCs and non-MCs, MCs consistently exhibit lower T_p in pre-ICME (4.5×10^4 K versus 6.3×10^4 K), sheath (10.1×10^4 K versus 12.8×10^4 K), and ME (2.8×10^4 K versus 3.1×10^4 K) regions, indicating that MCs are generally cooler. However, post-ICME T_p are comparable (7.5×10^4 K versus 7.7×10^4 K), suggesting similar recovery conditions (Table 1). N_p shows enhancement in the sheath and a drop in the ME, consistent with expectations from shock compression and subsequent expansion (Fig. 6c). The sheath has a median N_p of 8.6 cm^{-3} for all ICMEs, decreasing to 5.3 cm^{-3} in the ME. Interestingly, MCs show even higher N_p in the sheath (11.4 cm^{-3}) and ME (6.3 cm^{-3}), compared to non-MCs (7.2 and 5.0 cm^{-3}, respectively). This implies that MCs are more strongly compressed and carry denser plasma.

The plasma beta (β), which is the ratio of thermal to magnetic pressure, shows an inverse relationship to T_p (Fig. 6d). All ICMEs show a sheath β of 1.1, dropping significantly to 0.5 in the ME, indicating magnetic dominance. MCs have an even lower β (0.3) than non-MCs (0.7), reinforcing the idea that MCs are more magnetically dominated and this aligns with the magnetic field strength B (Fig. 6e). For all ICMEs, the pre-ICME region has a median B of 8.6 nT, comparable to 8.5 nT in the ME. For MCs, the ME region has an even stronger B of 11.3 nT, while non-MCs show a lower 7.1 nT, highlighting the stronger magnetic core in MCs. Notably, V patterns also reveal interesting differences. Non-MCs tend to propagate faster, with ME speeds of 438 km s^{-1} compared to 421 km s^{-1} for MCs. In the sheath, non-MCs are at 479 km s^{-1} versus 455 km s^{-1} for MCs (Fig. 6f). Despite these slower speeds, MCs show higher dynamic pressure ($P_{\rm dyn}$) in both the sheath (4.9 nPa versus 3.4 nPa) and ME (2.2 versus 1.9 nPa) (Fig. 6g).

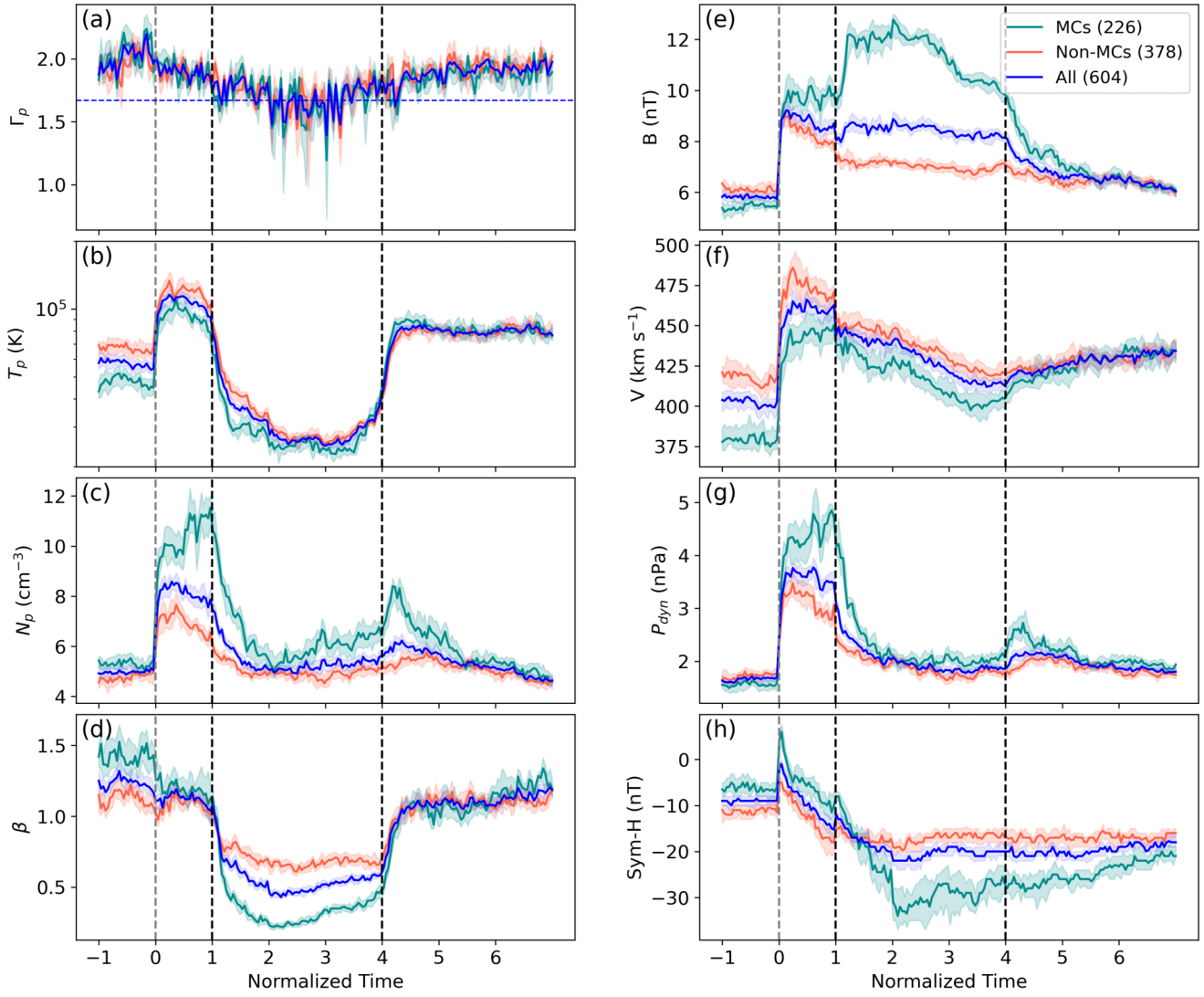

Figure 6. SEA showing the median values of parameters across the pre-ICME, sheath, ME, and post-ICME regions: (a) polytropic index (Γ_p), (b) proton temperature (T_p), (c) proton number density (N_p), (d) plasma beta (β), (e) magnetic field strength (B), (f) flow speed (V), (g) dynamic pressure ($P_{\rm dyn}$), and (h) geomagnetic index (Sym-H). The curves represent: teal for MC, orange for non-MC, and blue for all MEs. Black vertical dashed lines mark the boundaries for the ME region, and grey dashed vertical lines mark the starting sheath region. The background colour-shaded regions represent the 68 per cent (1σ) confidence intervals obtained via bootstrap resampling.

Interestingly, the consistently higher $P_{\rm dyn}$ observed in the sheath regions of MCs indicates stronger momentum fluxes associated with these structures. This elevated pressure at the shock arrival often results in a sharp positive spike in the Sym-H index, a phenomenon known as SSC (L. F. Burlaga & K. W. Ogilvie 1969; B. Veenadhari et al. 2012). Our analysis shows that this positive excursion in Sym-H is generally more prominent for MCs than for non-MCs (Fig. 6h). Following the SSC, the Sym-H index typically decreases as the ME passes, particularly when strong southward magnetic fields are present, enhancing magnetic reconnection and intensifying GS activity (J. W. Dungey 1961; B. T. Tsurutani & W. D. Gonzalez 1997; Y. Kamide et al. 1997). While the rate of Sym-H decline in the sheath region is comparable between MCs and non-MCs, a notable difference emerges in the ME region, where MCs exhibit a steeper drop and reach lower minimum Sym-H values. This pattern, initial high $P_{\rm dyn}$ in the sheath triggering SSC, followed by a significant drop in Sym-H during the ME phase, is consistent with the established sequence of GS development. It is evident that MCs tend to produce stronger SSCs and drive more intense GS compared to non-MCs (C.-C. Wu & R. P. Lepping 2007; E. Echer et al. 2008). Moreover, once the ICME reaches its minimum Sym-H value during the main phase of the storm, the subsequent recovery back to positive values or levels similar to the post-ICME region tends to take longer for MCs than for non-MCs (Fig. 6h). This slower recovery suggests a more prolonged disturbance to Earth's magnetosphere following MC-driven storms.

Both MCs and non-MCs exhibit a similar $V_{\rm exp}$ of approximately 20 km s^{-1}, indicating that the overall radial growth of the ME structure is nearly identical across these two categories. To examine the internal structure of the ME more closely, we used the distortion parameter (DiP) as defined in T. Nieves-Chinchilla et al. (2018). Specifically, DiP-B quantifies the asymmetry in the magnetic field strength profile, while DiP-N is an analogous measure for the proton number density profile. A DiP value of 0.5 represents a perfectly

Table 1. Median value of plasma and magnetic field parameters of various regions associated with different categories of ME.

Category	Regions	Γ_p	T_p (10^4 K)	N_p (cm^{-3})	V (km s^{-1})	β	B (nT)	P_{dyn} (nPa)	DiP-B	DiP-N	V_{exp} (km s^{-1})
All ICME	Pre	2.02	5.3	5.0	400	1.2	8.6	1.7	–	–	–
	Sheath	1.83	11.5	8.6	469	1.1	9.3	3.8	–	–	–
	ME	1.74	3.0	5.3	433	0.5	8.5	2.0	0.48	0.48	21
	Post	1.91	7.6	5.4	428	1.1	6.6	2.0	–	–	–
MC	Pre	2.09	4.5	6.6	375	1.4	5.6	1.6	–	–	–
	Sheath	1.83	10.1	11.4	455	1.1	10.4	4.9	–	–	–
	ME	1.75	2.8	6.3	421	0.3	11.3	2.2	0.48	0.46	21
	Post	1.88	7.5	5.7	432	1.1	6.8	2.1	–	–	–
Non-MC	Pre	1.95	6.3	4.8	417	1.1	6.1	1.7	–	–	–
	Sheath	1.83	12.8	7.2	479	1.1	8.7	3.4	–	–	–
	ME	1.72	3.1	5.0	438	0.7	7.1	1.9	0.48	0.49	20
	Post	1.93	7.7	5.2	428	1.1	6.6	1.9	–	–	–
Heating MEs	Pre	1.84	6.2	5.0	423	1.0	6.6	1.8	–	–	–
	Sheath	1.64	15.3	7.7	505	0.9	10.2	4.0	–	–	–
	ME	0.42	3.1	5.0	454	0.5	8.3	2.2	0.47	0.46	24
	Post	1.59	8.6	4.9	448	1.0	6.7	2.0	–	–	–
Cooling MEs	Pre	2.16	4.9	5.0	377	1.3	5.5	1.6	–	–	–
	Sheath	1.99	9.3	9.4	437	1.2	8.3	3.7	–	–	–
	ME	2.07	2.9	5.6	412	0.5	8.5	2.0	0.49	0.49	19
	Post	2.14	6.8	5.7	410	1.1	6.6	2.0	–	–	–
High-impact ICMEs	Pre	1.97	9.1	7.3	422	1.1	6.8	1.8	–	–	–
	Sheath	1.56	58.4	17.2	676	1.0	22.8	14.5	–	–	–
	ME	0.59	4.5	3.2	615	0.1	13.4	3.0	0.30	0.38	70
	Post	1.21	10.8	3.1	573	0.8	6.2	2.0	–	–	–
Moderate-impact ICMEs	Pre	1.98	4.9	5.4	409	1.1	6.2	1.8	–	–	–
	Sheath	1.79	13.1	9.7	479	1.0	10.7	4.7	–	–	–
	ME	1.69	3.3	5.2	455	0.4	10.0	2.1	0.46	0.45	22
	Post	1.88	9.1	5.0	456	1.0	7.0	2.0	–	–	–

symmetric profile centred around the midpoint of the ME. Values less than 0.5 indicate stronger compression at the front portion of the ME, whereas values greater than 0.5 suggest compression toward the rear. For the entire set of ICMEs, we found that both DiP-B and DiP-N have median values of 0.48, implying a slight asymmetry with compression predominantly at the leading edge of the ME. Interestingly, when separating the events into MC and non-MC types, we observed that both have the same DiP-B value of 0.48, suggesting similar magnetic field asymmetry. However, there is a subtle difference in the density structure: MCs show a slightly lower DiP-N of 0.46 compared to 0.49 in non-MCs. This indicates that the density profile within MCs is more front-loaded and asymmetric, whereas non-MCs tend to have a more symmetric density distribution.

The SEA reveals systematic plasma and magnetic field variations across ICMEs, with clear differences between MCs and non-MCs. While both categories share broadly similar thermodynamic trends, such as elevated Γ_p in the pre- and post-ICME regions, sheath, and near-adiabatic cooling within the ME, MCs are distinguished by cooler temperatures, lower plasma β, stronger magnetic fields, denser plasma, and higher dynamic pressures, all of which contribute to more pronounced SSCs and deeper Sym-H depressions. Despite these differences, Γ_p distributions remain largely comparable between MCs and non-MCs, suggesting that magnetic topology alone does not govern ICME thermal evolution. These results motivate a closer examination of plasma behaviour in heating and cooling MEs, where thermodynamic states may provide additional insights into their geoeffectiveness.

5.2 Comparative plasma evolution in heating and cooling MEs

We performed a comparative SEA between heating and cooling MEs based on Γ_p, where MEs with $\Gamma_p < 1.67$ were categorized as heating and those with $\Gamma_p > 1.67$ as cooling MEs (Fig. 7). This classification reveals important physical differences in plasma and magnetic field behaviours between the two categories across all associated regions, pre-ICME, sheath, ME, and post-ICME, highlighting the underlying thermodynamic and dynamical processes that differentiate the two categories.

For heating MEs, the evolution of Γ_p shows a gradual decline from the pre-ICME region, where it has a median value of 1.84, to 1.64 in the sheath (Table 1). This decline becomes markedly steep within the MEs, where Γ_p reaches a median value of 0.42, indicating significant heating and deviation from adiabatic behaviour (Fig. 7a). Interestingly, Γ_p recovers partially in the post-ICMEs region to 1.59, suggesting the plasma begins to relax after the central heating phase in MEs. In contrast, cooling MEs exhibit consistently high values of Γ_p across all regions, starting from 2.16 in the pre-ICME wind, rising slightly to 2.14 post-ICME, with a minor dip to 2.07 within the ME. This consistently elevated Γ_p suggests an enhanced cooling evolution throughout the structure.

The statistical analysis reveals a clear and robust distinction in the distribution of Γ_p between heating and cooling MEs. The KS test yields a large test statistic ($D = 0.325$) and a p-value effectively equal to zero, indicating that the two distributions differ significantly in shape. The Mann–Whitney U test further supports this with $p < 10^{-10}$, confirming a statistically significant shift in central tendency without assuming Gaussian behaviour. Cliff's Delta of -0.361

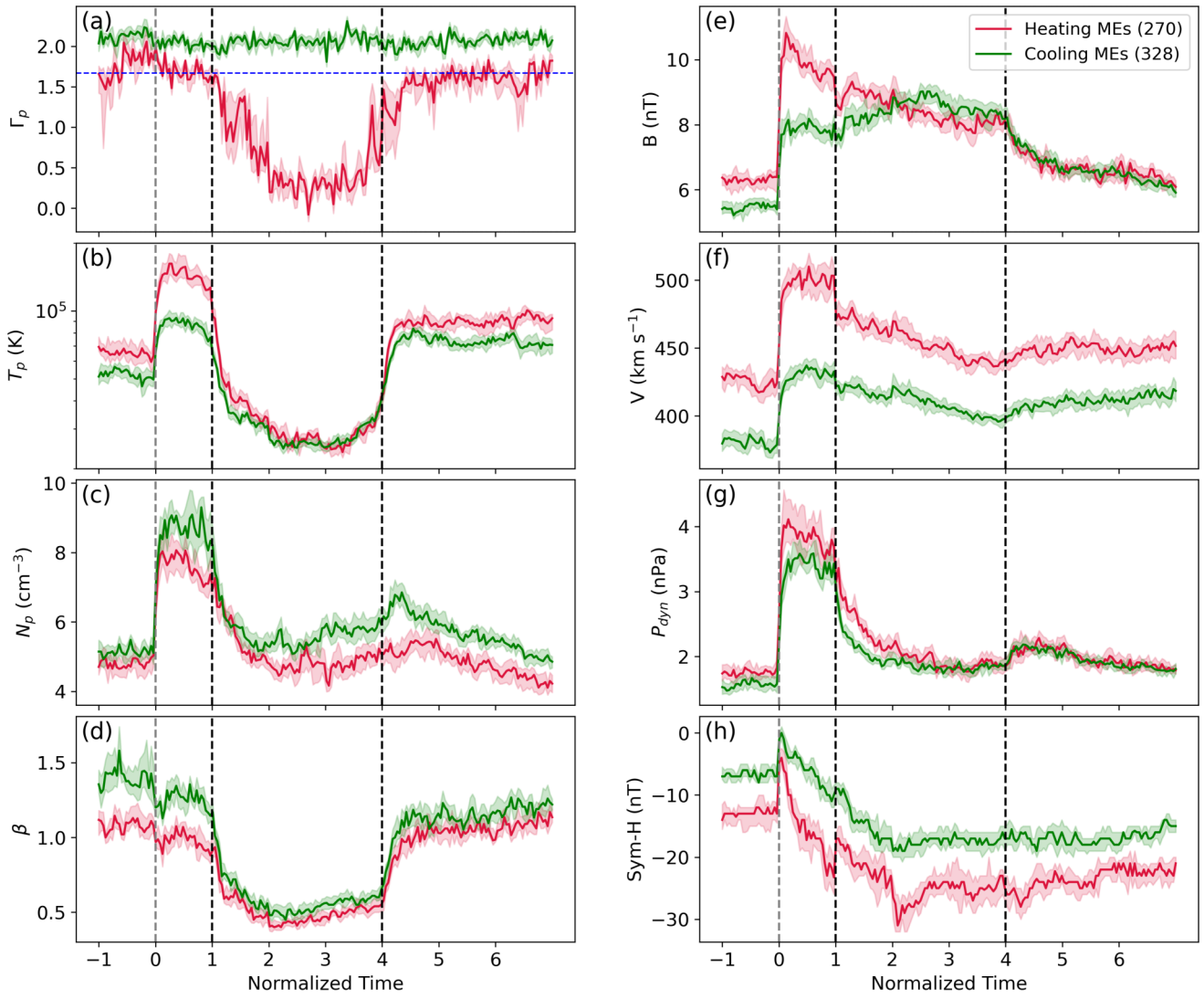

Figure 7. SEA showing the median values of parameters across the pre-ICME, sheath, ME, and post-ICME regions: (a) polytropic index (Γ_p), (b) proton temperature (T_p), (c) proton number density (N_p), (d) plasma beta (β), (e) magnetic field strength (B), (f) flow speed (V), (g) dynamic pressure ($P_{\rm dyn}$), and (h) geomagnetic index (Sym-H). The curves represent: red for heating ME and green for cooling ME. Black vertical dashed lines mark the boundaries for the ME region, and grey dashed vertical lines mark the starting sheath region. The background colour-shaded regions represent the 68 per cent (1σ) confidence intervals obtained via bootstrap resampling.

indicates a medium to large effect size, meaning that a randomly selected cooling ME has a higher Γ_p than a randomly selected heating ME 68 per cent of the time. This trend is corroborated by the KDE plot (Fig. C1b), where the cooling population peaks sharply around $\Gamma_p \approx 2$, whereas the heating population exhibits a broader, bimodal structure with enhanced density at lower Γ_p values (near 0), indicative of more compressive or subadiabatic behaviour. Additionally, a permutation test on the median Γ_p values provides additional confirmation: the observed median difference between heating and cooling MEs is substantial ($\Delta\Gamma_p = -1.82$), with a p-value effectively zero, reinforcing that this difference is not attributable to random variation. Collectively, these results strongly suggest that heating MEs are characterized by lower polytropic indices, indicative of enhanced internal energy deposition, while cooling MEs tend to follow more adiabatic or thermally relaxing trajectories.

We noticed that T_p profile trends reinforce this distinction. Heating MEs show a substantial increase in the sheath region (15.3×10^4 K) compared to the pre-ICME SW (6.2×10^4 K), implying shock or compression-induced heating at the leading edge of the disturbance (Table 1). While temperature falls to 3.1×10^4 K inside the ME, typical for ME interiors, the extremely low Γ_p here reveals that this low temperature compared to surrounding regions is not due to adiabatic cooling but possibly due to non-adiabatic energy exchange. The post-ICME region sees a T_p rebound to 8.6×10^4 K. On the other hand, cooling MEs show a smoother T_p evolution: starting at 4.9×10^4 K pre-ICME, rising to 9.3×10^4 K in the sheath, and dropping to 2.9×10^4 K within the MEs, followed by a rise to 6.8×10^4 K post-ICME. The cooling is more uniform, matching the stable high values of Γ_p (> 1.67) across all the regions. Further, N_p illustrates this contrast. In heating MEs, N_p rises from 5.0 cm^{-3} in pre-ICME to 7.7 cm^{-3} in the sheath due to compression, then drops within the ME (5.0 cm^{-3}) and remains nearly steady post-ICME (4.9 cm^{-3}). The cooling events, however, start with a slightly higher pre-ICME density (5.0 cm^{-3}), see a much larger increase in the sheath (9.4 cm^{-3}), and retain a moderately higher density inside the ME (5.6 cm^{-3}) and

post-ICME (5.7 cm^{-3}), consistent with weaker expansion and stronger compression overall (Fig. 7).

Furthermore, B remains high in the sheath of both categories, 10.2 nT for heating and 8.3 nT for cooling MEs, which could be due to compression but falls within the ME (Fig. 7e). However, the cooling MEs exhibit a slightly higher median field strength (8.5 nT) inside the ME than the heating ones (8.3 nT), which supports the idea of less expansion and greater field preservation. Heating MEs have a consistently higher flow speed V throughout the event, starting from 423 km s^{-1} and peaking at 505 km s^{-1} in the sheath. Inside the MEs region, the flow slows slightly to 454 km s^{-1} and has an expected expansion-driven decreasing trend, with a further drop to 448 km s^{-1} in the post-region. Cooling MEs begin at a lower speed of 377 km s^{-1}, rise to 437 km s^{-1} in the sheath, and fall to 410 km s^{-1} in the ME and post-regions. This suggests heating MEs experience stronger expansion, whereas cooling MEs retain a more compact, slower-moving structure. Noticeably, the β profile in the heating and cooling ME categories reveals a common pattern inside the MEs and post-ICME regions but diverges notably in the pre-ICME and sheath regions. In heating MEs, β remains around 1.05 before and after the event, dips to 0.94 in the sheath, and drops further to 0.48 within the ME, reflecting the expected dominance of magnetic pressure in the ejecta and a return to typical SW conditions afterward. Cooling MEs, on the other hand, exhibit a sharper decline in β inside the ME (0.5) from higher values in both the pre-ICME (1.3) and post-ICME (1.1) regions. However, the key distinction lies in the upstream and sheath regions: cooling MEs are preceded by less magnetically dominated plasma, consistent with their weaker magnetic fields observed in those regions (Fig. 7).

P_{dyn} trends mirror the velocity evolution, peaking in the sheath for both categories, 4.0 nPa in heating and 3.6 nPa in cooling, then declining within the MEs and post-ICMEs regions. Notably, heating MEs maintain similar post-ICME dynamic pressure (2.0 nPa) to cooling MEs (2.0 nPa) despite differences in V and N_p. Interestingly, despite the stronger P_{dyn} in heating MEs, we note that cooling MEs tend to produce a more substantial spike in Sym-H at the moment of SSC associated with shock arrival, suggesting that factors beyond P_{dyn} such as strength and orientation of magnetic field in the pre-MEs regions also play an important role in the observed SSC. However, carefully examining, we can see that the jump in the Sym-H from the pre-MEs is certainly larger for heating MEs than cooling MEs, consistent with the magnetospheric compression related to increased dynamic pressure at the arrival of shock ahead of MEs (Fig. 7).

Furthermore, the Sym-H index declines as the sheath and ME pass (Fig. 7h). The rate of this decline is notably steeper in the sheath region for heating MEs compared to cooling MEs, suggesting a more rapid onset of magnetic reconnection and geomagnetic disturbance during the early phase of storm development. Furthermore, heating MEs exhibit lower Sym-H minima within the MEs region, reflecting their tendency to drive a stronger GS. This is consistent with the elevated magnetic field strengths observed in the sheath and front portion of MEs for heating MEs. During the recovery phase, when the MEs exit and SW conditions begin to normalize, both heating and cooling MEs show a similar pattern towards the recovery phase. This suggests that the post-ICME SW environment is almost the same, regardless of the heating or cooling behaviour of the preceding MEs. Notably, pre-ICME regions associated with heating MEs show stronger negative Sym-H values compared to cooling MEs. This implies a more disturbed magnetospheric environment even before the heating MEs structure, potentially due to other preceding SW structures. Taken together, the stronger P_{dyn}, deeper Sym-H depressions, and more pronounced pre- and post-event activity are noted for heating MEs than cooling MEs.

We also note that heating MEs have a slightly higher V_{exp} of 24 km s^{-1} while cooling MEs expand slowly at just 19 km s^{-1}. Although the contrast is not strong, this indicates that heating MEs undergoing stronger radial expansion are leading to cooling suppression and energy retention within the ME, which is also found for CMEs close to the Sun in the study of S. Khuntia et al. (2024). The distortion parameters (DiP-B and DiP-N) for heating and cooling MEs both hover close to 0.5, indicating relatively symmetric internal structures (Table 1). However, Heating MEs show slightly lower DiP values (0.47 for DiP-B and 0.46 for DiP-N), suggesting a mild compression toward the front of the ME. In contrast, cooling MEs have marginally higher values (both 0.49), pointing to a near-central symmetry with a slight tendency for rear-side compression. This subtle difference hints that heating MEs may be more dynamically evolving or compressed by the upstream SW, while cooling MEs, being more magnetically organized, retain a more balanced structure across their radial span.

Overall, heating and cooling MEs exhibit fundamentally distinct thermodynamic and plasma signatures. Heating MEs are marked by very low Γ_p, stronger compression, higher speeds, enhanced expansion, and deeper Sym-H depressions, making them more geoeffective drivers of GS. In contrast, cooling MEs evolve with consistently high Γ_p, weaker expansion, and more uniform plasma behaviour, reflecting enhanced cooling and greater magnetic flux preservation. These contrasting behaviours highlight the importance of thermal state in shaping ICME–magnetosphere interactions and motivate further investigation into how such plasma evolution varies across GS classes.

5.3 Variation in plasma evolution across different storms classes

To better understand the geoeffectiveness of ICMEs, we classified events into two categories based on their geomagnetic impacts: (i) high-impact ICMEs driving storms with Sym-H < -200 nT and (ii) moderate-impact ICMEs driving storms with -200 nT <Sym-H < -50 nT. We intentionally excluded events with Sym-H > -50 nT, as these weak cases may dilute the median profiles and obscure meaningful trends in the plasma and magnetic field parameters. This classification is motivated to highlight how variations in SW and ICMEs properties, particularly in thermal and magnetic parameters, can be connected to the intensity of storms.

Our analysis indicates a noticeable distinction in thermodynamic behaviour (Γ_p) of high- and moderate-impact ICMEs (Fig. 8a). In high-impact ICMEs, Γ_p drops significantly from 1.97 in the pre-ICME region to 1.56 in the sheath and even further to 0.59 within the MEs before moderately rising to 1.21 in the post-ICME region (Table 1). This steep decline during the MEs reflects enhanced heating processes within the magnetic structure. Noticeably, there are a lot of variations in Γ_p for high-impact ICMEs, indicating localized heating. For moderate-impact ICMEs, Γ_p also decreases across the ICME, from 1.98 (pre-ICME) to 1.79 (sheath), but remains consistently higher than the adiabatic index and compared to high-impact ICMEs. The ME region shows $\Gamma_p = 1.69$ for moderate-impact ICMEs, indicative of an adiabatic expansion. The post-ICME value of 1.88 reflects an enhanced cooling than adiabatic conditions. This contrast hints at somewhat more pronounced thermodynamic changes, perhaps due to stronger compression and greater magnetic energy dissipation, in high-impact ICMEs compared to their moderate-impact counterparts.

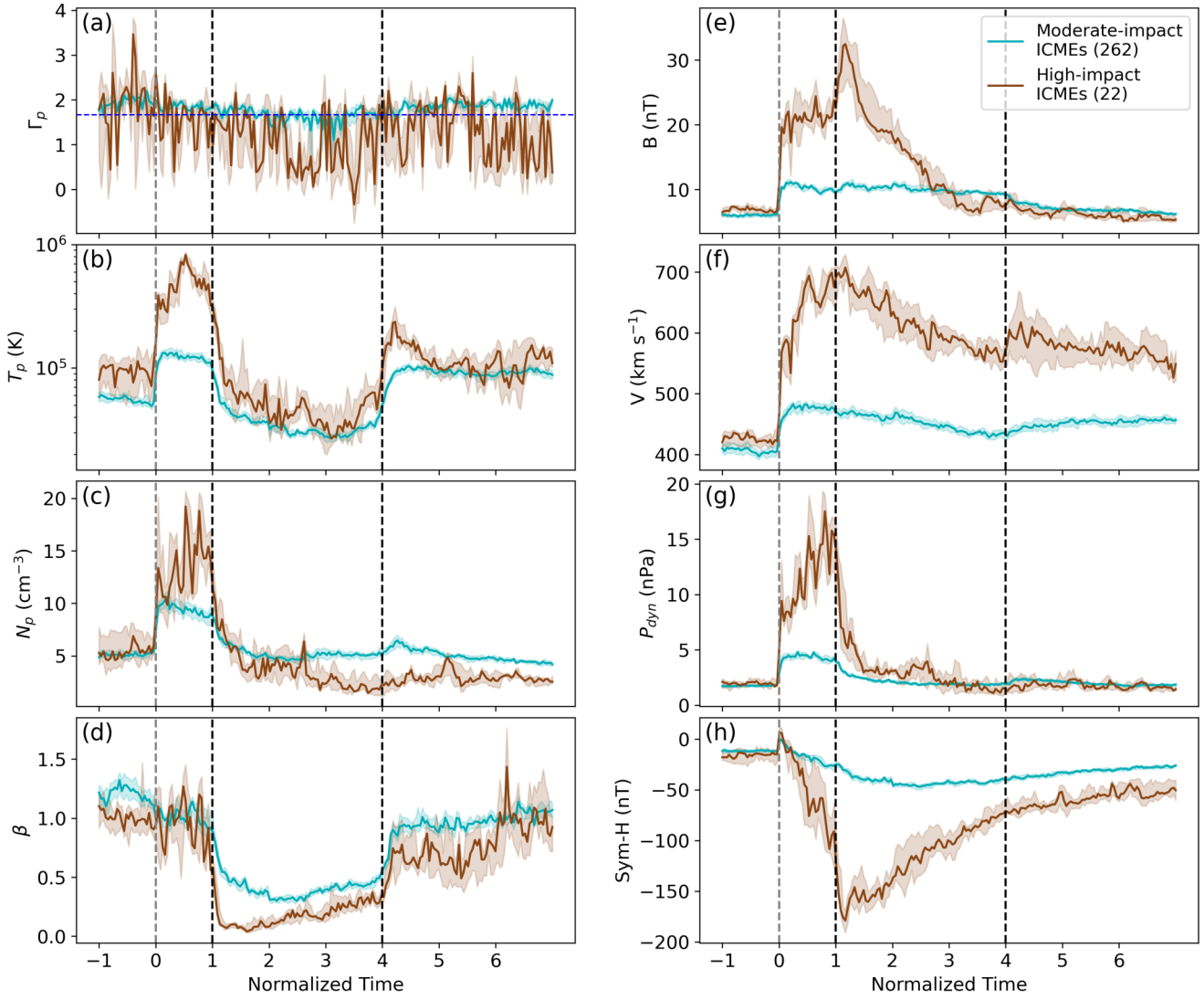

Figure 8. SEA showing the median values of parameters across the pre-ICME, sheath, ME, and post-ICME regions: (a) polytropic index (Γ_p), (b) proton temperature (T_p), (c) proton number density (N_p), (d) plasma beta (β), (e) magnetic field strength (B), (f) flow speed (V), (g) dynamic pressure ($P_{\rm dyn}$), and (h) geomagnetic index (Sym-H). The curves represent: teal for moderate-impact ICMEs and brown for high-impact ICMEs. Black vertical dashed lines mark the boundaries for the ME region, and grey dashed vertical lines mark the starting sheath region.The background colour-shaded regions represent the 68 per cent (1σ) confidence intervals obtained via bootstrap resampling.

The comparison between ME part of high- and moderate-impact ICMEs reveals statistically significant differences in the thermodynamic behaviour as characterized by Γ_p, although the effect size remains modest. The KS test yields a test statistic of $D = 0.106$ with a p-value of 9.52×10^{-98}, indicating a significant difference in the shape of the two Γ_p distributions. The Mann–Whitney U test supports this finding, with a p-value of 1.09×10^{-89}, suggesting a meaningful shift in central tendency. Cliff's Delta of -0.116 indicates a small effect size, showing that a randomly selected moderate-impact ICME has a higher Γ_p than a high-impact ICME in approximately 56 per cent of comparisons. This is consistent with the observed median difference of $\Delta\Gamma_p = -0.56$ between the two populations, which is statistically significant according to the permutation test ($p < 10^{-5}$). The KDE plot (Fig. C1c) illustrates this subtle but consistent separation, with moderate-impact events exhibiting a denser concentration in the higher-Γ_p regime. This trend is further reflected in the SEA: during the main storm phase, the proportion of time bins with $\Gamma_p < 1.67$ is substantially higher for high-impact events (66 per cent) compared to moderate-impact events (19 per cent), suggesting more prevalent heating in stronger storms. Conversely, moderate-impact ICMEs maintain $\Gamma_p > 1.67$ in 81 per cent of time bins, indicating more adiabatic behaviour. Taken together, these results indicate that high-impact ICMEs are statistically more likely to exhibit lower polytropic indices, which may be associated with stronger energy dissipation or internal heating processes contributing to their geoeffectiveness.

Noticeably, T_p exhibits a highly elevated peak in the sheath region for high-impact ICMEs, reaching a median of 58.4×10^4 K, compared to 13.1×10^4 K in moderate-impact ICMEs (Table 1). This dramatic heating in strong events points to intense shock compression region ahead of MEs. In the pre-ICME region, T_p is also higher in high-impact ICMEs (9.1×10^4 K) than in moderate-impact ones (5.0×10^4 K), suggesting a hotter upstream environment. Inside the ME, the temperature decreases substantially in both cases, to 4.5×10^4 K (high-impact) and 3.3×10^4 K (moderate-impact), consistent with the expected expansion-related cooling of

the magnetically dominated ejecta. The post-ICME region shows similarly elevated levels as 10.8×10^4 K for high-impact versus 9.1×10^4 K for moderate-impact ICMEs. Moreover, N_p follows an expected pattern of enhancement in the sheath region and dilution inside the MEs, but with key differences in magnitude. In high-impact MEs, the sheath region shows a sharp rise to 17.1 cm^{-3} from 7.3 cm^{-3} in the pre-ME region, followed by a significant drop to 3.1 cm^{-3} within the MEs and remaining low at 3.1 cm^{-3} post-MEs. In contrast, moderate-impact ICMEs exhibit a less dense sheath (9.7 cm^{-3}) and maintain higher density in MEs (5.2 cm^{-3}) and post-MEs density (5.0 cm^{-3}). This indicates that strong events are accompanied by more efficient plasma compression in the sheath but more depleted interiors, consistent with stronger expansion effects.

Notably, β clearly differentiates the magnetic dominance in ME regions between the drivers of two storm categories (Fig. 8d). For high-impact ICMEs, β plunges from 1.1 (pre-ICME region) and 1.0 (sheath) to a remarkably low 0.1 inside the MEs before rising to 0.8 post-ICME region. Moderate-impact ICMEs follow a similar trend but with much milder variation, maintaining values of 1.1 (pre-ICME), 1.0 (sheath), 0.4 (ME), and 1.0 (post-ICME). The significantly lower β within MEs of high-impact ICMEs reflects stronger magnetic pressure and flux content, contributing directly to enhanced storm-driving potential. We found that B is markedly higher in high-impact ICMEs, peaking at 22.8 nT in the sheath and 13.4 nT in the MEs, compared to 10.7 nT in the sheath and 10.1 nT in MEs driving moderate-impact ICMEs (Fig. 8e). Interestingly, inside the MEs of high-impact ICMEs, B decreases rapidly from leading to the trailing edge of MEs. This is also evident in the DiP-B parameters, which have a value of 0.30, indicating stronger magnetic compression close to the leading part of ME (Table 1). However, the DiP-N = 0.38 suggests a density compression but as front-loaded as magnetic compression. This asymmetry in high-impact ICMEs is likely a consequence of stronger dynamic interactions with the ambient SW and enhanced expansion, leading to sharper, more compressed fronts and more depleted trailing regions. DiP-B = 0.46 and DiP-N = 0.45 suggest a more symmetrical magnetic field and density inside ME of moderate-impact ICMEs than the high-impact ones. These elevated magnetic field strengths in the sheath and MEs are crucial for the development of strong GS, particularly when associated with sustained southward components.

As expected, V is significantly higher in high-impact ICMEs, indicating faster propagating ICMEs (Fig. 8f). V increases from 422 km s^{-1} (pre) to 676 km s^{-1} in the sheath, peaks at 615 km s^{-1} inside the ME, and remains elevated at 573 km s^{-1} post-ICME. Moderate-impact ICMEs, by contrast, feature more subdued speeds: 409 km s^{-1} (pre), 479 km s^{-1} (sheath), 455 km s^{-1} (ME), and 456 km s^{-1} (post). The sharp speed enhancements in high-impact ICMEs are indicative of greater kinetic energy and geoeffectiveness, which are often associated with fast CMEs. Notably, V_{exp} is substantially greater in high-impact ICMEs, with a median value of 70 km s^{-1} compared to 22 km s^{-1} in moderate-impact ICMEs. This increased expansion suggests a higher internal pressure and a dynamically evolving structure. We found that P_{dyn} shows an extreme increase during the sheath phase of high-impact ICMEs, reaching 14.5 nPa, an increase from the pre-ICME level of 1.8 nPa. It then drops to 3.0 nPa in the ME and further to 2.0 nPa in post-ICME region. Moderate-impact ICMEs also show a sheath enhancement (4.7 nPa from 1.8 nPa in pre-ICME), but the ME and post-ICME values (2.1 and 2.0 nPa, respectively) are more stable. This difference indicates that the initial SW compression of the magnetosphere due to high-impact ICMEs is much more intense than moderate-impact ICMEs.

The Sym-H index, which reflects geomagnetic response, displays an obviously distinct behaviour between high- and moderate-impact ICMEs, particularly around and after storm onset (Fig. 8h). In the pre-ICME region, both categories of ICMEs exhibit nearly identical Sym-H levels, indicating similar quiet geomagnetic conditions prior to the arrival of the disturbances. Following this, both types of ICMEs show a comparable sudden positive spike in Sym-H (SSC) despite the significantly stronger P_{dyn} associated with the shock driven by high-impact ICMEs. This suggests that SSC magnitude may depend on other coupling conditions beyond P_{dyn} alone. A sharp drop in Sym-H follows in the sheath region, where high-impact ICMEs show a much steeper and deeper descent, indicating stronger magnetic reconnection and more effective energy transfer to the magnetosphere. Notably, the lowest Sym-H value, marking the main phase of the storm, occurs near the leading edge of the MEs for high-impact ICMEs. Notably, the recovery phase of the storms caused by high-impact ICMEs typically begins shortly after the leading edge of the ME and extends throughout the remaining ME and post-ICME region.

Although the geomagnetic response is primarily driven by B_z and P_{dyn} (E. Echer et al. 2008; I. G. Richardson & H. V. Cane 2011; M.-X. Zhao et al. 2021), our results show that these parameters are intrinsically connected to the thermodynamic state of the ICME, as described by Γ_p. The lower Γ_p values observed in high-impact ICMEs imply enhanced heat retention or ongoing energy input, which maintains higher internal pressure and magnetic tension within the ejecta. Such overpressured MEs behave as stronger pistons, compressing the upstream SW more effectively and generating intense sheath regions with amplified magnetic fields. Through field-line draping and flux pile-up, this compression can locally enhance and rotate B_z (W. B. Manchester et al. 2004; W. Manchester et al. 2017), thereby strengthening magnetospheric coupling and deepening the storm main phase. In contrast, moderate-impact ICMEs, characterized by higher and more adiabatic Γ_p, expand more freely, resulting in weaker sheath compression, reduced magnetic field amplification, and lower dynamic pressure at 1 au. Hence, the thermodynamic state of the ejecta can regulate how kinetic and magnetic energy are partitioned and transferred to the magnetosphere. The observed relationship between low Γ_p, high internal pressure, and enhanced magnetic compression provides a thermodynamic basis for the greater geoeffectiveness of high-impact ICMEs. Future event-specific studies will aim to quantify the relative contributions of these heating-related processes to magnetic field amplification and storm intensity, thereby establishing a more direct link between CME thermal evolution and geoeffective potential.

6 CONCLUSION

This study provides a comprehensive thermal characterization of MEs and associated plasma properties across solar cycles 23, 24, and the rising phase of 25, based on the behaviour of the polytropic index (Γ_p). By categorizing MEs into heating and cooling types, and applying a refined classification scheme (major-heating, isothermal, adiabatic, and major-cooling), we uncover critical insights into their solar-cycle dependence, thermodynamic evolution, plasma signatures, and geoeffectiveness. The main conclusions are as follows:

(i) Heating MEs dominate during solar maxima and descending phases (especially in SC23), reflecting strong thermal energy input during eruption and/or interplanetary propagation. In contrast, the rising phases of SC23, SC24, and SC25 show a predominance of cooling MEs, suggesting reduced heating efficiency or different source-region conditions.

(ii) A progressive increase in median Γ_p values from 1.46 in SC23 to 1.87 in SC24 indicates a shift from heating- to cooling-dominated thermal states in MEs. The fraction of heating MEs decreases from approximately 59 per cent in SC23 to 34 per cent in SC24, suggesting that this change could arise either from inherent differences in the MEs near the Sun or from their altered evolution during transit.

(iii) The refined classification using Γ_p (e.g. major-heating, isothermal, adiabatic, major-and cooling) shows that MEs rarely behave adiabatically or isothermally; they are thermodynamically active systems. The majority of MEs show extreme values of Γ_p (<0.9 or >1.77), highlighting intense energy exchange, either strong energy gain or significant thermal loss.

(iv) Heating MEs exhibit strong solar cycle modulation in Γ_p, T_p, and $V_{\rm exp}$, indicating active and variable heating processes tied to solar activity levels and eruption energetics. Their Γ_p shows large year-to-year variation with distinct lower values (strong heating) near solar maxima and minima phases, especially in SC23 and SC24. Despite low *in-situ* T_p in some years (e.g. 2013), high $V_{\rm exp}$ and low Γ_p indicate significant in-transit heating, suggesting that initial eruption condition and evolution en route jointly determine ME thermal states.

(v) Cooling MEs remain thermodynamically stable and consistent across cycles, with nearly constant $\Gamma_p \approx 2$, suggesting enhanced cooling beyond what is expected from natural adiabatic expansion. Interestingly, despite their cooling behaviour, cooling MEs exhibit T_p values comparable to those of heating MEs, suggesting that they either originate with higher internal energy or retain substantial thermal energy during their interplanetary propagation before reaching 1 au.

(vi) More geoeffective ICMEs are typically MCs, characterized by strong magnetic fields, low plasma beta, and distinct thermal properties such as low proton temperatures and $\Gamma_p < 1.67$. Their coherent magnetic structure and dominant magnetic pressure often lead to deeper Sym-H depressions compared to those linked with non-MC ICMEs.

(vii) Heating and cooling MEs evolve through fundamentally different thermodynamic pathways: heating MEs exhibit pronounced non-adiabatic behaviour, characterized by very low Γ_p, along with elevated dynamic and magnetic pressures, significant internal energy deposition, and enhanced geoeffectiveness. Moreover, heating MEs exhibit front-loaded compression, asymmetry in internal density structure (low DiP), and faster expansion speeds. In contrast, cooling MEs are found to exceed adiabatic expectations (high Γ_p), maintain magnetic coherence, and result in milder geomagnetic responses.

(viii) High-impact ICMEs are typically heating MEs (primarily MCs) ($\Gamma_p = 0.59$), showing stronger magnetic fields, low plasma beta, higher bulk and expansion speeds, and stronger dynamic compression in the sheath region. The thermal state of MEs, alongside their other geoeffective properties, may be a good indicator of the ICME's potential to drive strong GS. Importantly, stronger storms caused by high-impact ICMEs often result not only from the properties of the ME itself but also from significant contributions by the preceding sheath structures.

Overall, our findings highlight the importance of incorporating the thermal state of ICMEs, alongside conventional plasma parameters, to gain deeper insights into their interplanetary evolution, classification, and potential geoeffectiveness at 1 au. The Γ_p-based framework, and its statistical characterization at 1 au, offers a novel perspective on CME energetics and provides a useful diagnostic for probing the underlying thermodynamic processes. However, such thermodynamic diagnostics (e.g. Γ_p) should not be interpreted in isolation as direct indicators of geoeffectiveness; rather, they must be assessed in conjunction with other plasma and magnetic field parameters. Only through such combined diagnostics can the role of CME thermal evolution in shaping geomagnetic responses be meaningfully constrained. Looking forward, this approach may support the development of improved space weather forecasting schemes and motivate further investigations into the physical drivers of CME heating and cooling in the heliosphere.

ACKNOWLEDGEMENTS

We appreciate the anonymous referee for the constructive comments and valuable suggestions. We acknowledge the use of data from the OMNI solar-wind database, compiled by the Space Physics Data Facility at NASA Goddard Space Flight Center.

DATA AVAILABILITY

All the observational input data sets used in this study are publicly available at NASA Coordinated Data Analysis Web (CDAWeb; https://cdaweb.gsfc.nasa.gov/).

REFERENCES

Akmal A., Raymond J. C., Vourlidas A., Thompson B., Ciaravella A., Ko Y. K., Uzzo M., Wu R., 2001, ApJ, 553, 922
Antonucci E. et al., 1997, ApJ, 490, L183
Baker D. N., 2009, Space Weather, 7, 02003
Bemporad A., Mancuso S., 2010, ApJ, 720, 130
Bemporad A., Raymond J., Poletto G., Romoli M., 2007, ApJ, 655, 576
Burlaga L. F., Ogilvie K. W., 1969, J. Geophys. Res., 74, 2815
Burlaga L., Sittler E., Mariani F., Schwenn R., 1981, J. Geophys. Res., 86, 6673
Burlaga L. F., Klein L., Sheeley N. R., Jr., Michels D. J., Howard R. A., Koomen M. J., Schwenn R., Rosenbauer H., 1982, Geophys. Res. Lett., 9, 1317
Cai J., Zhang L., Jiang C., Yan K., Feng X., Zuo P., Wang Y., 2025, MNRAS, 538, 2569
Cane H. V., Richardson I. G., 2003, J. Geophys. Res.: Space Phys., 108 1156
Cane H. V., Richardson I. G., Wibberenz G., 1997, J. Geophys. Res., 102, 7075
Cane H. V., Richardson I. G., St. Cyr O. C., 2000, Geophys. Res. Lett., 27, 3591
Cao J., Ma Y., Parks G., Reme H., Dandouras I., Zhang T., 2013, J. Geophys. Res. Space Phys., 118, 313
Chi Y., Shen C., Wang Y., Xu M., Ye P., Wang S., 2016, Sol. Phys., 291, 2419
Ciaravella A., Raymond J. C., Reale F., Strachan L., Peres G., 2001, ApJ, 557, 351
Cliver E. W., Ling A. G., 2001, ApJ, 556, 432
Dasso S., Mandrini C. H., Démoulin P., Luoni M. L., 2006, A&A, 455, 349
Desai R. T., Zhang H., Davies E. E., Stawarz J. E., Mico-Gomez J., Iváñez-Ballesteros P., 2020, Sol. Phys., 295, 130
Domingo V., Fleck B., Poland A. I., 1995, Sol. Phys., 162, 1
Dungey J. W., 1961, Phys. Rev. Lett., 6, 47
Echer E., Gonzalez W. D., Tsurutani B. T., Gonzalez A. L. C., 2008, J. Geophys. Res. Space Phys., 113, A05221
Farrugia C. J., Freeman M. P., Burlaga L. F., Lepping R. P., Takahashi K., 1993, J. Geophys. Res., 98, 7657
Filippov B., Koutchmy S., 2002, Sol. Phys., 208, 283
Gonzalez W. D., Joselyn J. A., Kamide Y., Kroehl H. W., Rostoker G., Tsurutani B. T., Vasyliunas V. M., 1994, J. Geophys. Res., 99, 5771
Gopalswamy N., 2006, J. Astrophys. Astron., 27, 243
Gopalswamy N., Akiyama S., Yashiro S., Xie H., Mäkelä P., Michalek G., 2014, Geophys. Res. Lett., 41, 2673
Gopalswamy N., Makela P., Akiyama S., Yashiro S., Thakur N., 2015, Sun Geosph., 10, 111

Gopalswamy N., Yashiro S., Akiyama S., 2016, ApJ, 823, L15
Gopalswamy N., Akiyama S., Yashiro S., 2020, ApJ, 897, L1
Gosling J. T., 1990, Geophys. Monogr. Ser., 58, 343
Gosling J. T., 1993, J. Geophys. Res., 98, 18937
Gosling J. T., Baker D. N., Bame S. J., Feldman W. C., Zwickl R. D., Smith E. J., 1987, J. Geophys. Res., 92, 8519
Gruesbeck J. R., Lepri S. T., Zurbuchen T. H., Antiochos S. K., 2011, ApJ, 730, 103
Gu C., Yao S., Dai L., 2020, ApJ, 900, 123
Guo X., Florinski V., Wang C., Ghanbari K., 2021, ApJ, 910, 99
Henke T. et al., 1998, Geophys. Res. Lett., 25, 3465
Janvier M. et al., 2019, J. Geophys. Res. Space Phys., 124, 812
Jian L., Russell C. T., Luhmann J. G., Skoug R. M., 2006, Sol. Phys., 239, 393
Jian L. K., Russell C. T., Luhmann J. G., Galvin A. B., 2018, ApJ, 855, 114
Kaiser M. L., 2005, Adv. Space Res., 36, 1483
Kamide Y. et al., 1997, Geophys. Monogr. Ser., 98, 1
Kasper J. C., Lazarus A. J., Steinberg J. T., Ogilvie K. W., Szabo A., 2006, J. Geophys. Res. Space Phys., 111, A03105
Katsavrias C., Nicolaou G., Livadiotis G., Vourlidas A., Wilson III L. B., Sandberg I., 2025, A&A, 695, A146
Khuntia S., Mishra W., 2025, J. Astrophys. Astron., 46, 70
Khuntia S., Mishra W., Mishra S. K., Wang Y., Zhang J., Lyu S., 2023, ApJ, 958, 92
Khuntia S., Mishra W., Wang Y., Mishra S. K., Nieves-Chinchilla T., Lyu S., 2024, MNRAS, 535, 2585
Khuntia S., Mishra W., Agarwal A., 2025, A&A, 698, A79
Kilpua E. K. J., Jian L. K., Li Y., Luhmann J. G., Russell C. T., 2011, J. Atmos. Sol.-Terr. Phys., 73, 1228
King J. H., Papitashvili N. E., 2005, J. Geophys. Res. Space Phys., 110, A02104
Ko Y.-K., Raymond J. C., Vršnak B., Vujić E., 2010, ApJ, 722, 625
Kumar A., Rust D. M., 1996, J. Geophys. Res., 101, 15667
Kuźma B., Brchnelova M., Perri B., Baratashvili T., Zhang F., Lani A., Poedts S., 2023, ApJ, 942, 31
Lamy P. L., Floyd O., Boclet B., Wojak J., Gilardy H., Barlyaeva T., 2019, Space Sci. Rev., 215, 39
Landi E., Raymond J. C., Miralles M. P., Hara H., 2010, ApJ, 711, 75
Larson D. E. et al., 1997, Geophys. Res. Lett., 24, 1911
Lee J. Y., Raymond J. C., Ko Y. K., Kim K. S., 2009, ApJ, 692, 1271
Lee J.-Y., Raymond J. C., Reeves K. K., Moon Y.-J., Kim K.-S., 2017, ApJ, 844, 3
Lepping R. P. et al., 1995, Space Sci. Rev., 71, 207
Lepri S. T., Zurbuchen T. H., Fisk L. A., Richardson I. G., Cane H. V., Gloeckler G., 2001, J. Geophys. Res., 106, 29231
Lepri S. T., Laming J. M., Rakowski C. E., von Steiger R., 2012, ApJ, 760, 105
Lepri S. T., Landi E., Zurbuchen T. H., 2013, ApJ, 768, 94
Lin J., Wang F., Deng L., Deng H., Mei Y., Zhang X., 2023, ApJ, 958, 1
Liou K. et al., 2014, J. Atmos. Sol.-Terr. Phys., 121, 32
Liu Y., Richardson J. D., Belcher J. W., 2005, Planet. Space Sci., 53, 3
Liu Y., Richardson J. D., Belcher J. W., Kasper J. C., Elliott H. A., 2006, J. Geophys. Res. Space Phys., 111, A01102
Liu Y., Thernisien A., Luhmann J. G., Vourlidas A., Davies J. A., Lin R. P., Bale S. D., 2010, ApJ, 722, 1762
Liu Y., Shen F., Yang Y., Ma M., 2022, ApJ, 940, 11
Lugaz N., Farrugia C. J., 2014, Geophys. Res. Lett., 41, 769
Lugaz N., Farrugia C. J., Manchester W. B. I., Schwadron N., 2013, ApJ, 778, 20
Luhmann J. G., Li Y., Arge C. N., Gazis P. R., Ulrich R., 2002, J. Geophys. Res. Space Phys., 107, 1154
Manchester W. B., Gombosi T. I., Roussev I., Ridley A., de Zeeuw D. L., Sokolov I. V., Powell K. G., Tóth G., 2004, J. Geophys. Res. Space Phys., 109, A02107
Manchester W., Kilpua E. K. J., Liu Y. D., Lugaz N., Riley P., Török T., Vršnak B., 2017, Space Sci. Rev., 212, 1159
Masías-Meza J. J., Dasso S., Démoulin P., Rodriguez L., Janvier M., 2016, A&A, 592, A118
Mayank P., Vaidya B., Chakrabarty D., 2022, ApJS, 262, 23
Mishra W., Srivastava N., 2013, ApJ, 772, 70
Mishra W., Srivastava N., 2014, ApJ, 794, 64
Mishra W., Teriaca L., 2023, J. Astrophys. Astron., 44, 20
Mishra W., Wang Y., Srivastava N., Shen C., 2017, ApJS, 232, 5
Mishra W., Srivastava N., Wang Y., Mirtoshev Z., Zhang J., Liu R., 2019, MNRAS, 486, 4671
Mishra W., Doshi U., Srivastava N., 2021, Front. Astron. Space Sci., 8, 142
Mishra W., Sahani P. S., Khuntia S., Chakrabarty D., 2024, MNRAS, 530, 3171
Montgomery M. D., Asbridge J. R., Bame S. J., Feldman W. C., 1974, J. Geophys. Res., 79, 3103
Möstl C. et al., 2022, ApJL, 924, L6
Nicolaou G., Livadiotis G., Wicks R. T., 2019, Entropy, 21,997
Nicolaou G., Livadiotis G., Wicks R. T., Verscharen D., Maruca B. A., 2020, ApJ, 901, 26
Nieves-Chinchilla T., Vourlidas A., Raymond J. C., Linton M. G., Al-haddad N., Savani N. P., Szabo A., Hidalgo M. A., 2018, Sol. Phys., 293, 25
Nieves-Chinchilla T., Jian L. K., Balmaceda L., Vourlidas A., dos Santos L. F. G., Szabo A., 2019, Sol. Phys., 294, 89
Ogilvie K. W. et al., 1995, Space Sci. Rev., 71, 55
Oloketuyi J., Liu Y., Zhao M., 2019, ApJ, 874, 20
Osherovich V. A., Farrugia C. J., Burlaga L. F., Lepping R. P., Fainberg J., Stone R. G., 1993, J. Geophys. Res., 98, 15331
Owens M. J., Lockwood M., Barnard L. A., 2018, Space Weather, 16, 694
Pandey K., Chakrabarty D., Kumar A., Bhardwaj A., Biswal S., Hussey G. C., Yadav A. K., 2023, Adv. Space Res., 71, 5438
Pant V., Majumdar S., Patel R., Chauhan A., Banerjee D., Gopalswamy N., 2021, Front. Astron. Space Sci., 8, 73
Phillips J. L., Feldman W. C., Gosling J. T., Scime E. E., 1995, Adv. Space Res., 16, 10
Pulkkinen T., 2007, Living Rev. Sol. Phys., 4, 1
Rakowski C. E., Laming J. M., Lepri S. T., 2007, ApJ, 667, 602
Regnault F., Janvier M., Démoulin P., Auchère F., Strugarek A., Dasso S., Noûs C., 2020, J. Geophys. Res. Space Phys., 125, e28150
Reva A., Bogachev S., Loboda I., Kirichenko A., Ulyanov A., 2023, Sol. Phys., 298, 61
Richardson I. G., Cane H. V., 1995, J. Geophys. Res., 100, 23397
Richardson I. G., Cane H. V., 2010, Sol. Phys., 264, 189 (RC)
Richardson I. G., Cane H. V., 2011, Space Weather, 9, S07005
Richardson I. G., Cane H. V., 2012, J. Space Weather Space Climate, 2, A01
Richardson I. G., Cane H. V., Cliver E. W., 2002, J. Geophys. Res. Space Phys., 107, 1187
Richardson I., Cane H., 2024, Near-Earth Interplanetary Coronal Mass Ejections Since January 1996, Ver. 4. Harvard Dataverse Dataset
Riley P., Linker J. A., Mikić Z., Odstrcil D., Zurbuchen T. H., Lario D., Lepping R. P., 2003, J. Geophys. Res. Space Phys., 108, 1272
Ruffenach A. et al., 2012, J. Geophys Res. Space Phys., 117, A09101
Russell C. T., Shinde A. A., 2003, Sol. Phys., 216, 285
Scolini C. et al., 2020, ApJS, 247, 21
Song H., Li L., Sun Y., Lv Q., Zheng R., Chen Y., 2021, Sol. Phys., 296, 111
Srivastava N., Venkatakrishnan P., 2004, J. Geophys Res. Space Phys., 109, A10103
Stone E. C., Frandsen A. M., Mewaldt R. A., Christian E. R., Margolies D., Ormes J. F., Snow F., 1998, Space Sci. Rev., 86, 1
Temmer M., 2021, Living Rev. Sol. Phys., 18, 4
Temmer M. et al., 2023, Adv. Space Res., in press
Tsurutani B. T., Gonzalez W. D., 1997, Geophys. Monogr. Ser., 98, 77
Tsurutani B. T., Smith E. J., Gonzalez W. D., Tang F., Akasofu S. I., 1988, J. Geophys. Res., 93, 8519
Veenadhari B., Selvakumaran R., Singh R., Maurya A. K., Gopalswamy N., Kumar S., Kikuchi T., 2012, J. Geophys. Res. Space Phys., 117, A04210
Vourlidas A., Subramanian P., Dere K. P., Howard R. A., 2000, ApJ, 534, 456
Vourlidas A., Howard R. A., Esfandiari E., Patsourakos S., Yashiro S., Michalek G., 2011, ApJ, 730, 59
Vršnak B., Žic T., Falkenberg T. V., Möstl C., Vennerstrom S., Vrbanec D., 2010, A&A, 512, A43
Wang Y., Zhang J., Shen C., 2009, J. Geophys. Res. Space Phys., 114, A10104

Webb D. F., Howard T. A., 2012, Living Rev. Sol. Phys., 9, 3
Winslow R. M., Lugaz N., Philpott L. C., Schwadron N. A., Farrugia C. J., Anderson B. J., Smith C. W., 2015, J. Geophys. Res. Space Phys., 120, 6101
Winslow R. M., Lugaz N., Scolini C., Galvin A. B., 2021, ApJ, 916, 94
Wu C.-C., Lepping R. P., 2007, Sol. Phys., 242, 159
Wu C.-C., Lepping R. P., 2011, Sol. Phys., 269, 141
Wu C.-C., Lepping R. P., 2015, Sol. Phys., 290, 1243
Wu C. C., Wu S. T., Dryer M., 2004, Sol. Phys., 223, 259
Wu C. C., Lepping R. P., Gopalswamy N., 2006, Sol. Phys., 239, 449
Zhang G., Burlaga L. F., 1988, J. Geophys. Res., 93, 2511
Zhang J. et al., 2007, J. Geophys. Res. Space Phys., 112, A10102
Zhang J., Poomvises W., Richardson I. G., 2008, Geophys. Res. Lett., 35, L02109
Zhang M., Jokipii J. R., McKibben R. B., 2003, ApJ, 595, 493
Zhao M.-X., Le G.-M., Li Q., Liu G.-A., Mao T., 2021, Sol. Phys., 296, 66
Zurbuchen T. H., Richardson I. G., 2006, Space Sci. Rev., 123, 31

SUPPORTING INFORMATION

Supplementary data are available at *MNRAS* online.

table1.pdf

Please note: Oxford University Press is not responsible for the content or functionality of any supporting materials supplied by the authors. Any queries (other than missing material) should be directed to the corresponding author for the article.

APPENDIX A: LIST OF ALL STUDIED ICMES

Table A1. List of ICMEs studied from 1996 June to 2024 December, covering solar cycles 23 to the rising phase of 25. The table includes the corresponding derived median value of the polytropic index (Γ_p), median value of the uncertainty in Γ_p ($\Delta\Gamma_p$) due to fractional measurement uncertainties in proton density ($\delta N_p = 2$ per cent) and proton temperature ($\delta T_p = 5$ per cent), expansion speed ($V_{\rm exp}$), and distortion parameters for magnetic field (DiP-B) and proton number density (DiP-N).

No.	Disturbance time	ME start time	ME end time	ME type	Median Γ_p	Median $\Delta\Gamma_p$	$V_{\rm exp}$ (km s^{-1})	DiP-B	DiP-N
1	1996-07-01 13:20:00	1996-07-01 18:00:00	1996-07-02 11:00:00	2	2.459	0.57	12	0.522	0.525
2	1996-08-07 06:00:00	1996-08-07 12:00:00	1996-08-08 10:00:00	2	2.23	1.135	10	0.578	0.439
3	1996-12-23 16:00:00	1996-12-23 17:00:00	1996-12-25 11:00:00	2	2.032	0.725	53	0.589	0.515
4	1997-01-10 01:04:00	1997-01-10 04:00:00	1997-01-11 02:00:00	2	0.777	0.333	44	0.501	0.777
5	1997-02-09 13:21:00	1997-02-10 02:00:00	1997-02-10 19:00:00	2	2.117	0.46	32	0.52	0.195
6	1997-04-10 17:45:00	1997-04-11 06:00:00	1997-04-11 19:00:00	2	1.342	0.23	−7	0.467	0.521
7	1997-04-21 06:00:00	1997-04-21 10:00:00	1997-04-23 04:00:00	2	2.219	0.638	31	0.512	0.444
8	1997-05-15 01:59:00	1997-05-15 09:00:00	1997-05-16 00:00:00	2	1.967	0.395	−12	0.443	0.4
9	1997-05-26 09:57:00	1997-05-26 16:00:00	1997-05-27 10:00:00	2	1.936	0.564	11	0.495	0.443
10	1997-06-08 16:36:00	1997-06-08 18:00:00	1997-06-10 00:00:00	2	2.039	0.517	19	0.538	0.402

Notes. This table is available in its entirety in machine-readable format as a Supportinf Information. A portion is shown here for illustrative purposes, indicating the form and content. The date time format used in columns 2–4 is YYYY-MM-DD HH:MM.

APPENDIX B: ANNUAL DISTRIBUTION OF MAGNETIC EJECTA WITH VARIOUS THERMAL STATES AT 1 AU

Table B1. Annual distribution of ME with various thermal states at 1 au.

Year	Major-heating count (per cent)	Isothermal count (per cent)	Heating count (per cent)	Adiabatic count (per cent)	Major-cooling count (per cent)
1996	0 (0)	0 (0)	0 (0)	0 (0)	3 (100)
1997	1 (5)	0 (0)	1 (5)	1 (5)	19 (86)
1998	5 (14)	1 (3)	3 (8)	4 (11)	23 (64)
1999	11 (33)	0 (0)	2 (6)	6 (18)	14 (42)
2000	24 (48)	0 (0)	5 (10)	5 (10)	16 (32)
2001	29 (60)	0 (0)	9 (19)	2 (4)	8 (17)
2002	12 (46)	0 (0)	4 (15)	4 (15)	6 (23)
2003	9 (43)	0 (0)	2 (9)	3 (14)	7 (33)
2004	9 (43)	0 (0)	2 (10)	4 (19)	6 (29)
2005	20 (65)	0 (0)	7 (23)	2 (6)	2 (6)
2006	6 (46)	1 (8)	1 (8)	2 (15)	3 (23)
2007	1 (50)	0 (0)	0 (0)	0 (0)	1 (50)
2008	0 (0)	0 (0)	0 (0)	1 (33)	2 (67)
2009	2 (18)	0 (0)	1 (9)	3 (27)	5 (45)
2010	3 (20)	0 (0)	1 (7)	1 (7)	10 (67)
2011	5 (16)	0 (0)	2 (6)	5 (16)	20 (63)
2012	3 (9)	0 (0)	2 (6)	4 (12)	26 (74)
2013	8 (33)	0 (0)	0 (0)	3 (13)	13 (54)
2014	6 (30)	0 (0)	1 (5)	4 (20)	9 (45)
2015	10 (33)	0 (0)	4 (13)	3 (10)	13 (43)
2016	5 (38)	0 (0)	1 (8)	1 (8)	6 (46)
2017	1 (11)	0 (0)	1 (11)	1 (11)	6 (67)
2018	1 (13)	0 (0)	2 (25)	0 (0)	5 (63)
2019	1 (14)	0 (0)	0 (0)	0 (0)	6 (86)
2020	2 (50)	0 (0)	0 (0)	0 (0)	2 (50)
2021	0 (0)	0 (0)	0 (0)	0 (0)	10 (100)
2022	1 (5)	0 (0)	1 (5)	1 (5)	16 (84)
2023	1 (4)	0 (0)	5 (20)	4 (16)	15 (60)
2024	1 (4)	1 (4)	5 (19)	4 (15)	16 (59)

APPENDIX C: KERNEL DENSITY ESTIMATES OF POLYTROPIC INDEX FOR DIFFERENT ICME CLASSIFICATIONS

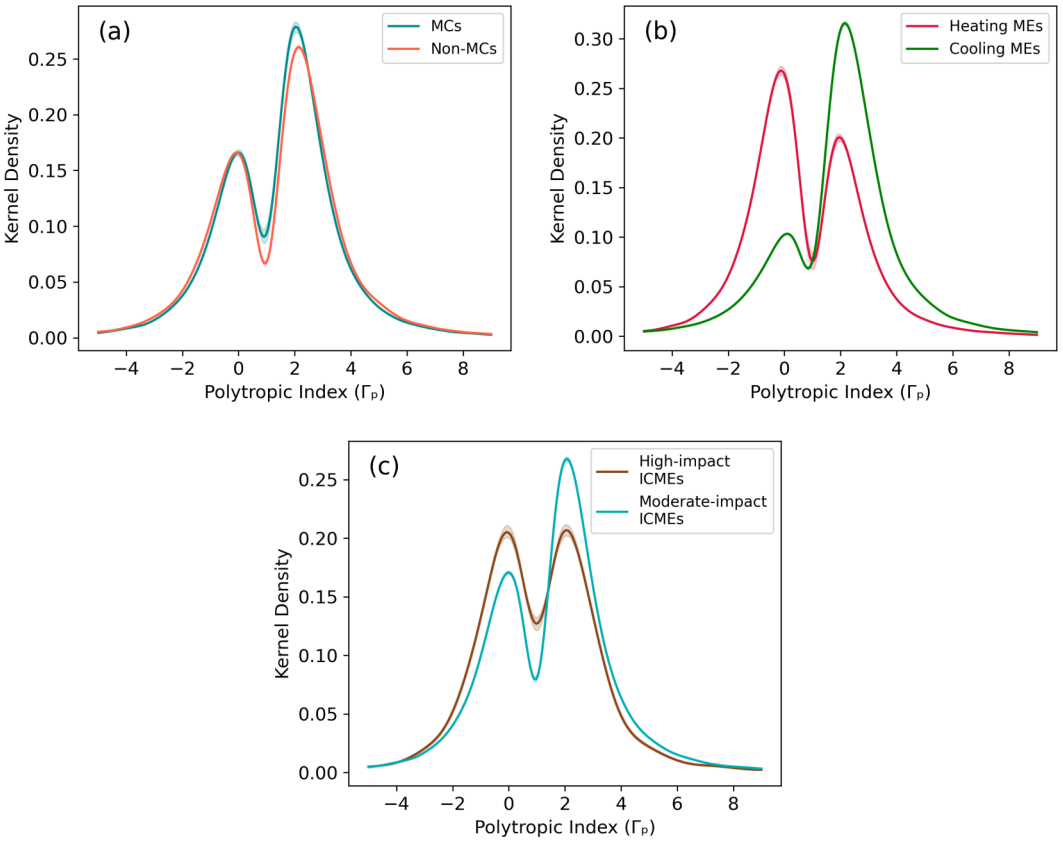

Figure C1. Comparison of Γ_p distributions using KDE plots with 68 per cent bootstrap confidence bands for ME part of (a) MCs versus non-MCs, (b) heating versus cooling MEs, and (c) high- versus moderate-impact ICMEs. These plots highlight differences in thermodynamic properties across ICME subsets.

This paper has been typeset from a TEX/LATEX file prepared by the author.